

Supplement of Atmos. Chem. Phys., 19, 139–163, 2019
<https://doi.org/10.5194/acp-19-139-2019-supplement>
© Author(s) 2019. This work is distributed under
the Creative Commons Attribution 4.0 License.



Supplement of

Dynamic changes in optical and chemical properties of tar ball aerosols by atmospheric photochemical aging

Chunlin Li et al.

Correspondence to: Yinon Rudich (yinon.rudich@weizmann.ac.il)

The copyright of individual parts of the supplement might differ from the CC BY 4.0 License.

Contents

1. Tar ball aerosol size distribution at downstream of the OFR (Figure S1)
2. OC-EC content of fresh polar and nonpolar tar ball aerosols
3. Fresh tar ball composition from HR-ToF-AMS measurement (Figure S2)
- 0 4. Summary of fresh tar ball particles chemical elemental ratios and effective densities (Table S1)
5. Aerodynamic size distribution for tar ball particles measured by SP-LD-REMPI-ToF-MS (Figure S3)
6. Exemplary aromatic compounds indicated by the mass spectra in Figure 3 (All listed substances are typical compounds in wood combustion emissions, Table S2)
7. Morphology of tar ball aerosols (Figure S4)
- 5 8. Refractive index for tar ball at mixture of 2:1 and 1:2 in volume of polar and nonpolar materials (Figure S5)
9. Example of absorption coefficients for some of the most absorbing PAHs identified in BBOA (Figure S6)
10. Methanol extractable BrC mass absorption cross sections (MAC) for fresh tar ball aerosols from 360 to 450 nm (Figure S7)
- 0 11. Mixing rules prediction for nonpolar-polar mixed tar ball aerosols (Figure S8-S12, Table S3-S4)
12. Summary of optical parameters for tar ball upon NO_x-dependent photochemical aging (Table S5)
13. Methanol extractable BrC mass absorption cross sections (MAC) for NO_x-free photochemical aged tar ball aerosols from 360 to 450 nm (Figure S13)
14. Optical and chemical changes for tar ball aerosols due to photolysis from UV light irradiation in the OFR (Table S6-S7, Figure S14-S17)
- 5 15. Optical and chemical changes of tar ball aerosols due to O₃ oxidation in the OFR (Figure S18-S19)
16. Mass spectra characters and effective density changes for tar ball particles upon photochemical oxidation (Table S8)
17. Detailed mass spectra changes for tar ball aerosols upon 6.7 EAD photochemical aging (Figure S20)
- 0 18. Standard AMS spectra for inorganic salt of NH₄NO₃ (Figure S21)
19. Detailed mass spectra changes for tar ball aerosols upon 4 EAD photochemical aging with 2.0 vol.% N₂O addition (Figure S22)
20. Methanol extractable BrC mass absorption cross section (MAC) for tar ball aerosols upon various NO_x-dependent photochemical aging processes (Figure S23)
- 5 21. Particle size- and light wavelength-resolved radiative forcing for tar ball aerosols oxidized via various NO_x-dependent oxidation processes (Figure S24-S25)

1. Tar ball aerosol size distribution at downstream of the OFR

Tar ball particles were generated via TSI atomizer, and concentration of tar ball particles was mediated in the OFR before these aerosols being photochemically oxidized. Polar, nonpolar, and mixture tar ball particles present similar size distributions.

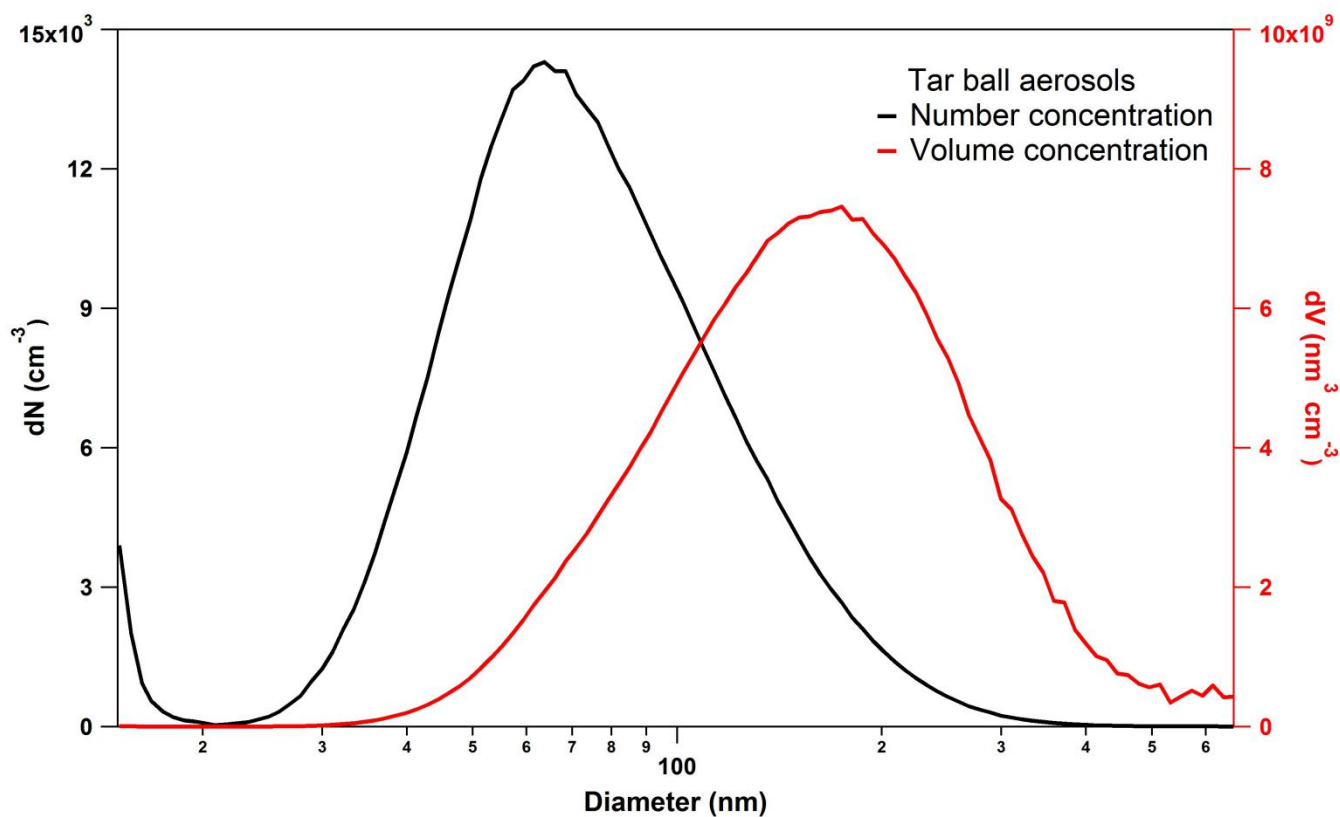


Figure S1. Size distribution of laboratory generated tar ball aerosols at downstream of the OFR. The distribution presents a narrow range with a single peak at ~70 nm diameter, similar to the size distribution of practical tar balls obtained from the wildfires and domestic biofuel burning (Pósfai et al., 2004; Chakrabarty et al., 2010).

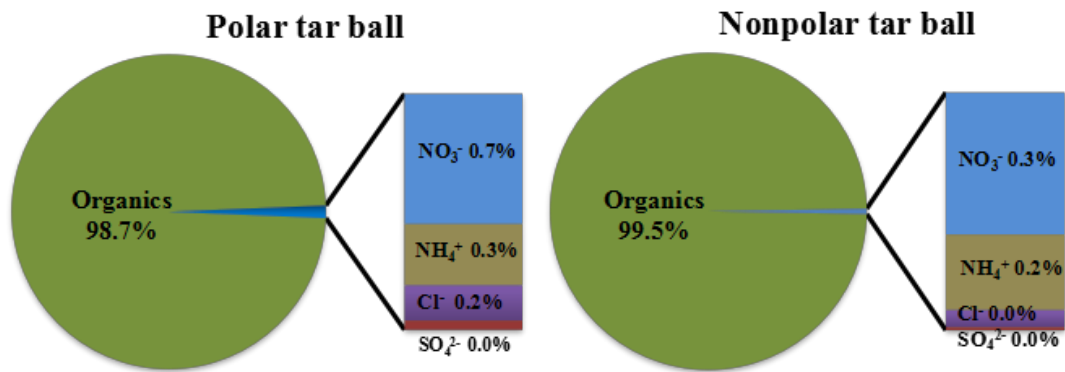
5 2. OC-EC content of fresh polar and nonpolar tar ball aerosols

Non-refractory organic carbon (OC) and refractory elemental carbon (EC) in fresh tar ball aerosols were analyzed using a DRI Model 2015 multi-wavelength thermal/optical carbon analyzer (Desert Research Institute, Nevada, USA) with the IMPROVE_A protocol (Chow et al., 2011; Li et al., 2018). In details, fresh nonpolar and polar tar balls were collected onto pretreated quartz filters (Whatman, Mainstone, UK, baked over 450 °C for 6 hr to eliminate any contamination), a circular punch (0.8 cm in diameter) of each loaded filter including operational blank filter was taken and analyzed. Four OC fractions (OC1, OC2, OC3, and OC4 correspond to gradient cutting temperature at 140, 280, 480, and 580 °C, respectively, in a helium atmosphere), three EC fractions (EC1, EC2, EC3 with cutting temperature of 590, 780, and 840 °C, respectively, in a 2% oxygen/98% helium atmosphere), and one PC fraction (pyrolyzed carbon content determined when transmitted laser returned to its original intensity after the sample was exposed to oxygen) were determined for each sample, and $OC=OC1+OC2+OC3+OC4+PC$, $EC=EC1+EC2+EC3-PC$, total carbon (TC) equals the sum of OC and EC. The blank-corrected and normalized carbon fractions for fresh tar ball aerosols were given below:

Tar ball	OC1	OC2	OC3	OC4	PC	EC1	EC2	EC3	OC	EC
Polar	38.8%	32.2%	18.4%	0.0%	10.6%	10.6%	0.0%	0.0%	100.0%	0.0%
Nonpolar	28.7%	25.8%	16.0%	7.7%	21.1%	21.7%	0.0%	0.0%	99.3%	0.7%

It is clear EC content was almost below detection limit for both polar- and nonpolar-tar balls, the slight EC fraction in nonpolar tar ball is less than 0.7% of TC content and resides in EC1, which can be termed as non-refractory char-EC, empirically defined as $EC1-PC$. Char-EC is stripped from some OC under oxygen-free heating during OC/EC measurement, which has much weak absorption, and thus can be distinguished as brown carbon rather than black carbon (Andreae and Gelencsér, 2006; Arora et al., 2015; Kim et al., 2011; Han et al., 2008, 2009). Many other studies on biomass burning emissions from wildfires and domestic burning have also reported negligible EC content in tar ball aerosols (Chakrabarty et al., 2010; Tivanski et al., 2007; Hand et al., 2005; China et al., 2013).

3. Fresh tar ball composition from HR-Tof-AMS measurement



5

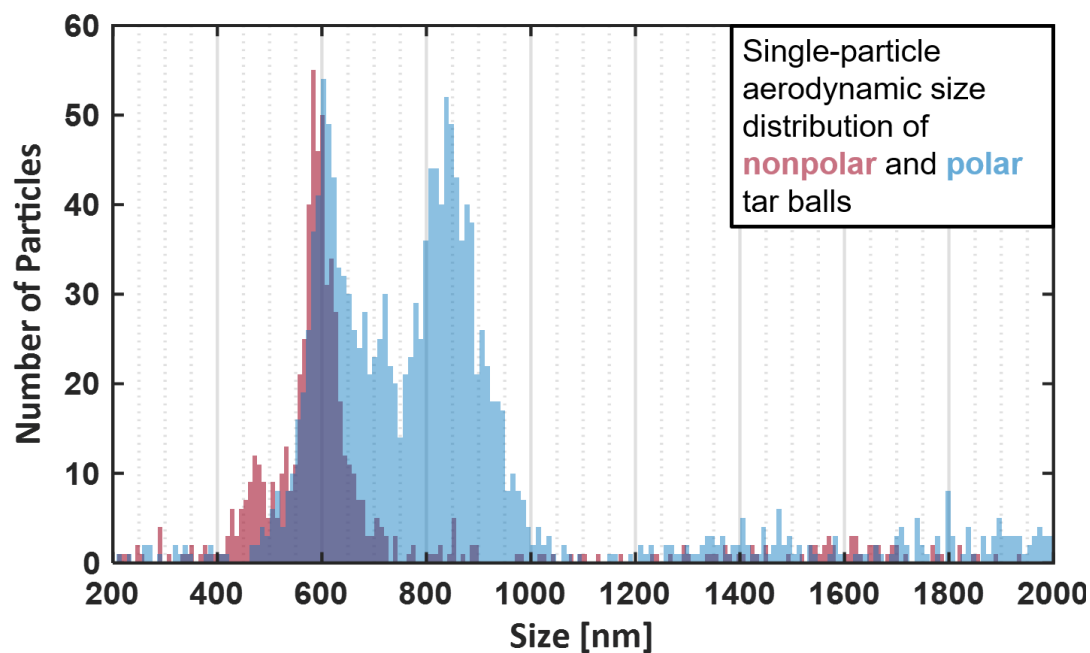
Figure S2. Fresh polar and nonpolar tar balls composition from HR-Tof-AMS measurement. Color mapping: organics-green, nitrates-blue, ammonium-yellow, chloride-purple, sulfates-red.

4. Organic elemental ratios for fresh tar ball aerosols were derived from AMS measurement at W mode, and effective densities of tar ball aerosols were calculated from aerodynamic diameter divided by mobility diameter assuming tar ball with sphericity of 1.0

Table S1. Summary of fresh tar ball particles chemical elemental ratios and effective densities

BBOA	Mass spectra			Density (g cm ⁻³)	Reference
	O:C	H:C	M/z>100 fraction		
Nonpolar	0.25±0.01	1.55±0.01	0.32	1.24±0.01	this work
Mixture (2:1 in vol.)	0.30±0.01	1.59±0.02	0.29	1.27±0.02	
Mixture (1:1 in vol.)	0.36±0.01	1.62±0.04	0.27	1.29±0.02	
Mixture (1:2 in vol.)	0.39±0.01	1.61±0.03	0.24	1.30±0.01	
Polar	0.44±0.02	1.64±0.03	0.15	1.33±0.02	
BBOA	0.3~0.4				Aiken et al., 2008
BBOA	0.29~0.33	1.51~1.58			Li et al., 2012
BBOA	0.18~0.26	1.4~1.5			He et al., 2010
BBOA	0.15~0.7	1.5~1.6	0.11~0.20	1.4	Zhou et al., 2017
BBOA				1.5	Sedlacek III et al., 2018
BBOA	0.33	1.90		1.18~1.19	Sumlin et al., 2017; 2018

5. Aerodynamic size distribution for tar ball particles measured by SP-LD-REMPI-ToF-MS



- 5 **Figure S3.** Particle aerodynamic size distributions for fresh nonpolar (red) and polar (blue) tar ball aerosols measured via laser velocimetry by the SP-LD-REMPI-ToF-MS instrument. The major mode peaks at about 550 nm for both particle classes while a second mode of larger particles occurs for polar tar balls and a second mode of smaller particles appears for nonpolar tar balls. Note that the detection efficiency drops rapidly below 250 nm due to the descending Mie scattering efficiency for particles much smaller than the wavelength (532 nm).

6. Exemplary Proper Polyaromatic Compounds indicated by the REMPI PAH Spectra in this study (Table S2)

Table S2. Exemplary proper (poly)aromatic compounds indicated by the REMPI PAH Spectra in Figure 3

m/z	Name	Formula	Polar tar ball	Nonpolar tar ball	BBOA Reference
110	Catechol	C ₆ H ₆ O ₂	√		Veres et al., 2010; Yee et al., 2013
115	PAHs fragments		√	√	Adler et al., 2011; Bruns et al., 2015
124	Guaiacol	C ₇ H ₈ O ₂	√		Li et al., 2017; Yee et al., 2013; Hoffmann et al., 2007
128	Naphthalene	C ₁₀ H ₈	√	√	Samburova et al., 2016; Passig et al., 2017; Bruns et al., 2015
138	4-Methylguajacol	C ₈ H ₁₀ O ₂	√	√	Adler et al., 2011; Yee et al., 2013
152	Vanillin	C ₈ H ₈ O ₃	√	√	Li et al., 2014; Passig et al., 2017; Yee et al., 2013; Hoffmann et al., 2007
	4-Ethylguajacol	C ₉ H ₁₂ O ₂			
158	Methoxynaphthalene	C ₁₁ H ₁₀ O	√		Santos et al., 2016; Yee et al., 2013; Hoffmann et al., 2007
	1,4-Naphthalenedione	C ₁₀ H ₆ O ₂			
	Methylnaphthol	C ₁₁ H ₁₀ O			
165	PAHs fragments		√	√	Adler et al., 2011; Bruns et al., 2015
168	4-Methylsyringol	C ₉ H ₁₂ O ₃	√		Santos et al., 2016; Hoffmann et al., 2007; Bruns et al., 2015
	Vanillic acid	C ₈ H ₈ O ₄			
178	Phenanthrene	C ₁₄ H ₁₀	√	√	Samburova et al., 2016; Bente et al., 2008, 2009; Passig et al., 2017
	Conifery aldehyde	C ₁₀ H ₁₀ O ₃			
182	Syringaldehyde	C ₉ H ₁₀ O ₄	√		Santos et al., 2016; Yee et al., 2013; Hoffmann et al., 2007
	4-Ethylsyringol	C ₁₀ H ₁₄ O ₃			
189, 190, 191	Retene fragments		√	√	Bente et al., 2008, 2009; Mandalakis et al., 2005
192	Methylphenanthrene	C ₁₅ H ₁₂	√	√	Samburova et al., 2016; Bente et al., 2008, 2009; Passig et al., 2017
202	Pyrene	C ₁₆ H ₁₀	√	√	Adler et al., 2011; Bente et al., 2008, 2009; Passig et al., 2017
	Fluoranthene				
203, 204, 205	Retene fragments		√	√	Passig et al., 2017; Mandalakis et al., 2005
206	Ethylphenanthrene	C ₁₆ H ₁₄		√	Samburova et al., 2016
219, 220	Retene fragments		√	√	Bente et al., 2008, 2009; Passig et al., 2017
234	Retene	C ₁₈ H ₁₈	√	√	Samburova et al., 2016; Bente et al., 2008, 2009; Passig et al., 2017

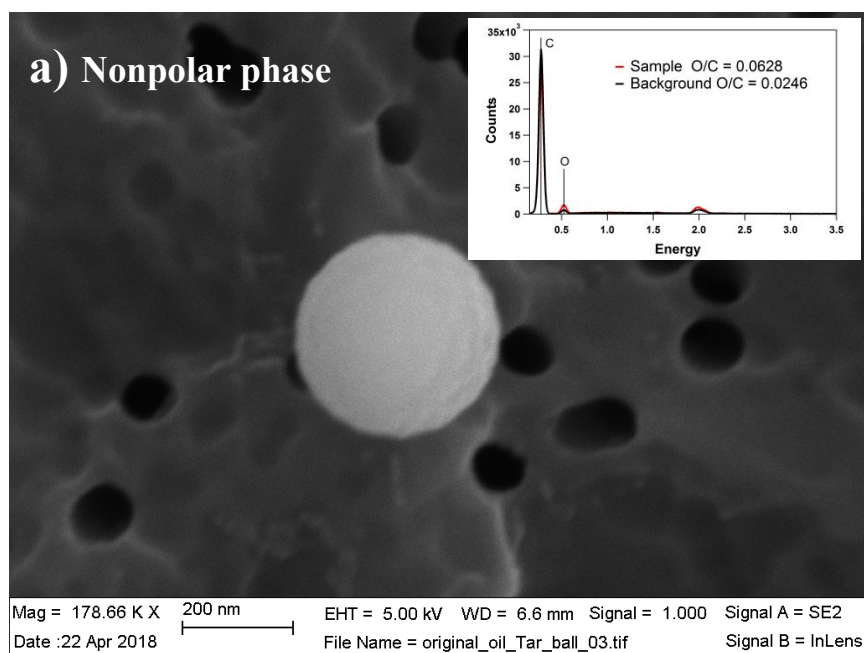
248	Methyl. Retene	C ₁₉ H ₂₀		√	Passig et al., 2017; Mandalakis et al., 2005
250	Ox. Retene	C ₁₈ H ₁₈ O	√	√	Samburova et al., 2016

Note: only some major and most proper aromatic compounds were listed in the table

7. Morphology of tar ball aerosols

5

0



5

0

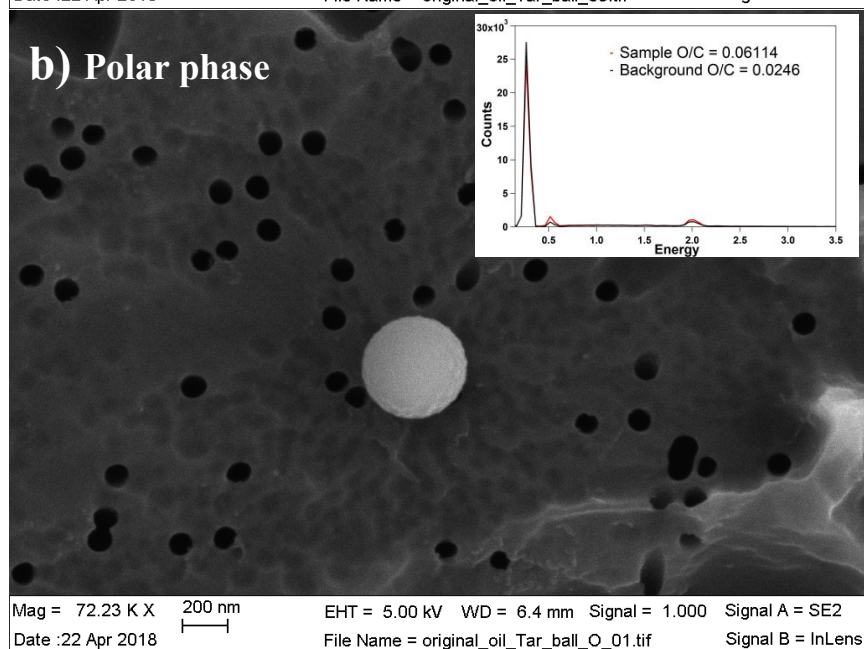


Figure S4. Morphology of fresh tar ball particles generated from polar and nonpolar phase tarry solutions. The particles are perfect spherical and amorphous in internal composition.

5

8. Refractive index for tar ball at mixture of 2:1 and 1:2 in volume of polar and nonpolar materials

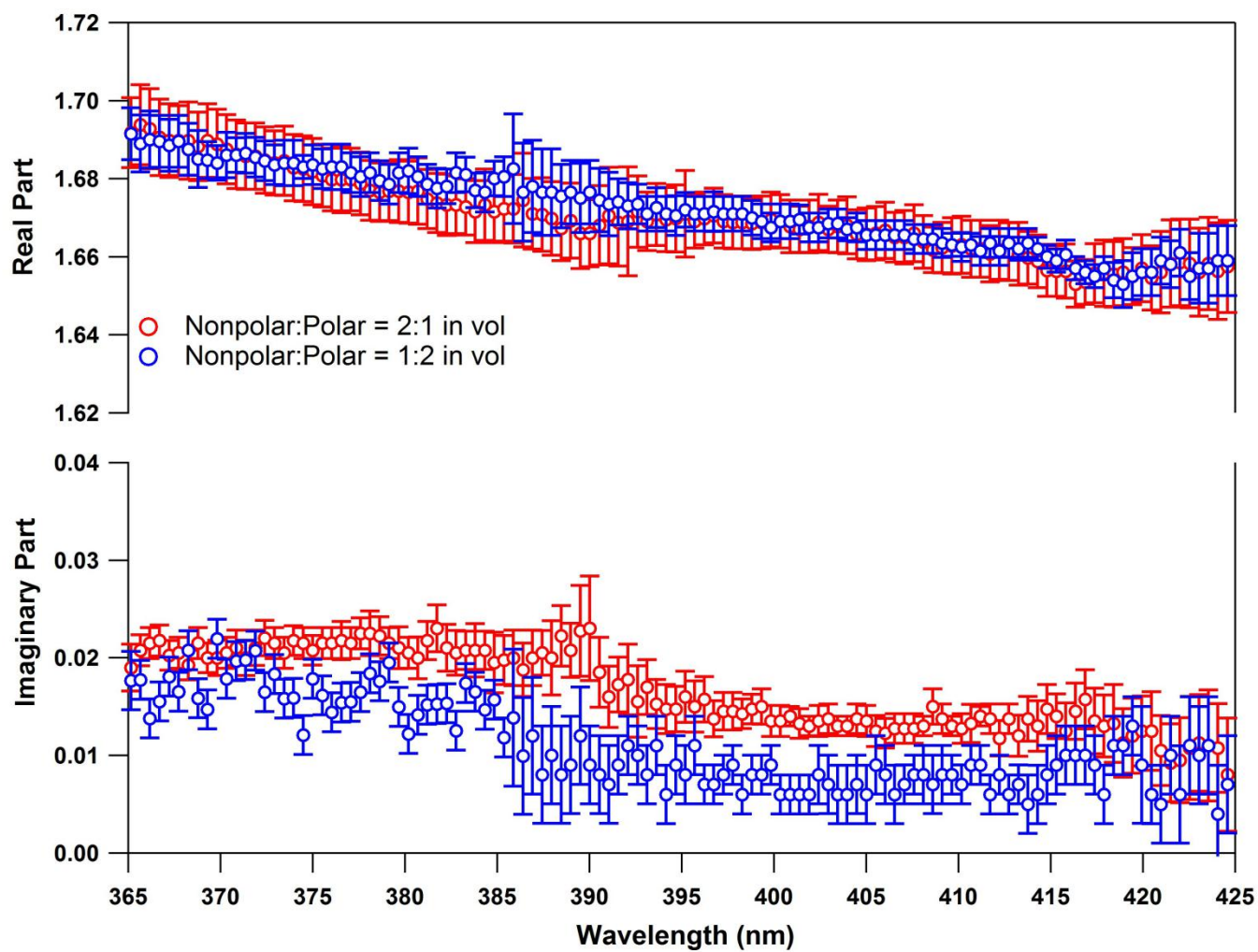


Figure S5. Wavelength-dependent refractive index (RI) for tar ball particles generated from polar and nonpolar phase solution mixtures

0

9. Example of absorption coefficients for some of the most absorbing PAHs identified in BBOA

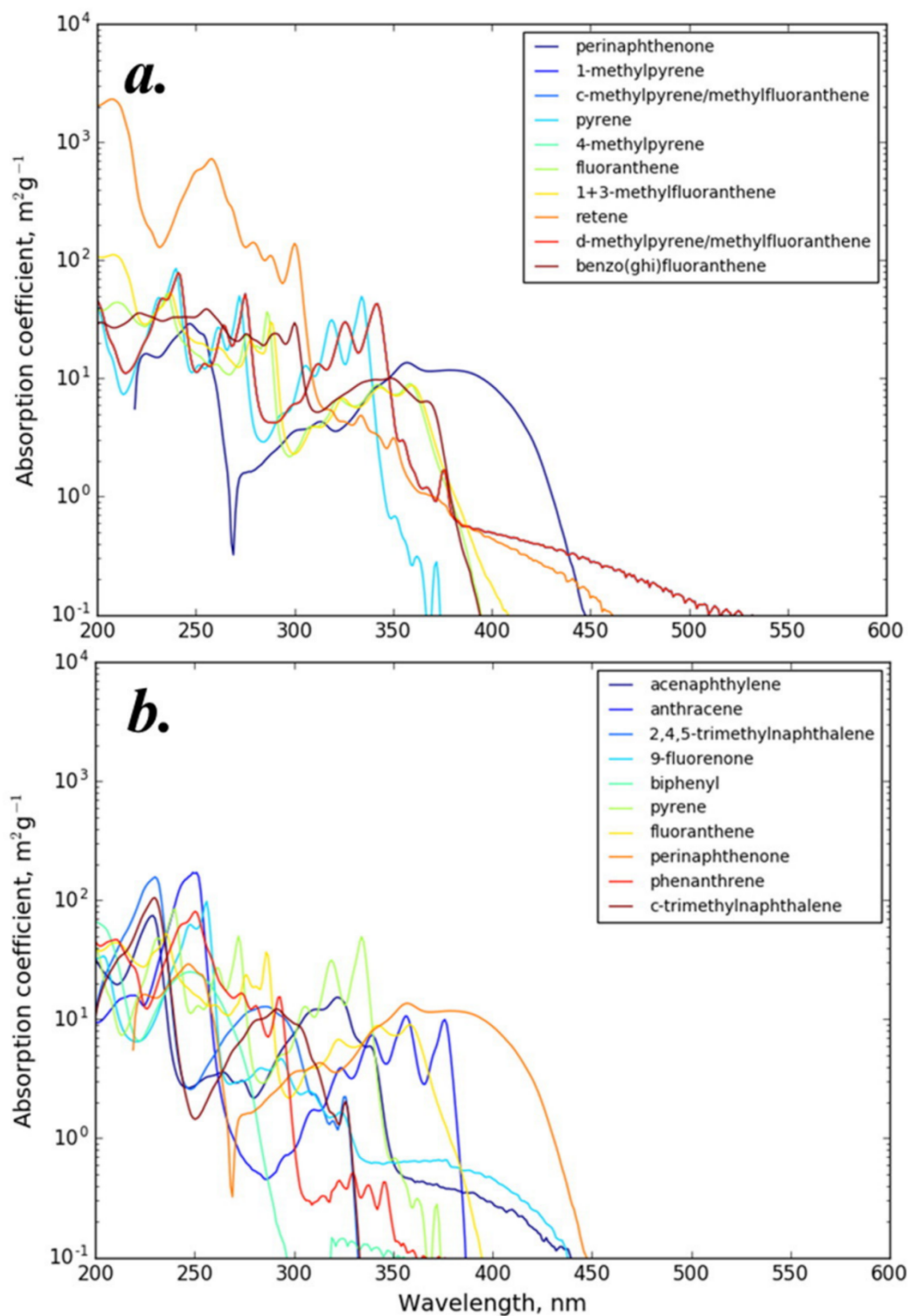


Figure S6. Absorption coefficients for some of the most absorbing PAHs identified in biomass burning emissions (Samburova et al., 2016).

10. Methanol extractable BrC mass absorption cross sections (MAC) for fresh tar ball aerosols from 360 to 450 nm

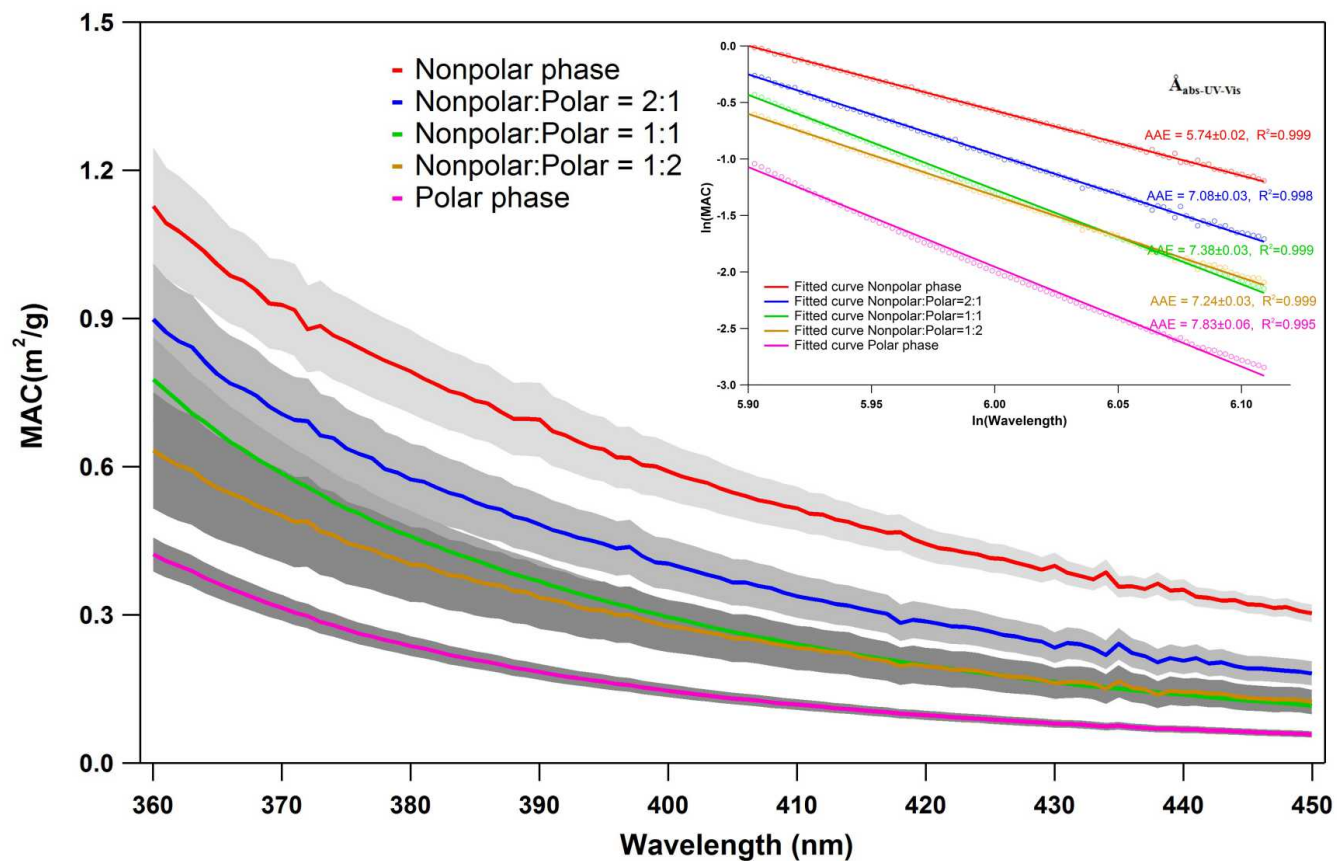


Figure S7. BrC mass absorption cross section (MAC) for methanol extracted fresh tar ball particles. Inset chart presents example of $\hat{A}_{\text{abs-UV-Vis}}$ calculated from natural logarithm regression of MAC and wavelength.

0 11. Prediction of mixture tar ball optical properties based on different mixing rules

There are many mixing rules currently in use to predict optical properties of aerosol from matrix of various substances: 1) molar refraction and absorption (Jacobson, 2002; Tang, 1997); 2) a volume-weighted linear average of the refractive indices (d'Almeida et al., 1991); 3) the Maxwell-Garnet rule (Chýlek et al., 1984); and 4) the dynamic effective medium approximation (Jacobson, 2006). Due to the complexity of undefined chemical composition of tar ball particles, the Maxwell-Garnet and dynamic effective medium approximation are not feasible in this study, therefore, the simple molar fraction and volume-weighted mixing rules were discussed to fit the optical results.

The “linear mixing rule” simplifies mixing state and interaction between matrix, assumes that total real and imaginary refractive indices of the mixture are result of the indices of the components weighted by their their volume fractions:

$$\begin{aligned} n_{tot} &= \sum_n f_i n_i \\ k_{tot} &= \sum_n f_i k_i \end{aligned} \quad [1]$$

0 Where f_i , n_i , and k_i are the volume fraction, real part, and imaginary part of each component

The molar fraction mixing rule assumes that the total molar refraction of a mixture is given by the linear average of the molar refraction of each component weighted by their molar volumes, i.e.,

$$\begin{aligned} \frac{\overline{M}}{\rho} \frac{n^2 - 1}{n^2 + 2} &= \sum_n \chi_i \frac{M_i}{\rho_i} \frac{n_i^2 - 1}{n_i^2 + 2} \\ \frac{\overline{M}}{\rho} k &= \sum_n \chi_i \frac{M_i}{\rho_i} k_i \\ \sum_n \chi_i &= 1 \end{aligned} \quad [2]$$

Where χ_i , M_i , and ρ_i are the molar fraction, molecular weight, and material density.

5 Refractive indices for tar ball generated from polar and nonpolar fraction mixture at solution mixing ratios of 1:2, 1:1, and 2:1 will be calculated from RI of polar and nonpolar optical results based on above two rules. The exact volume and molar fraction for bulk polar and nonpolar part in particles can be estimated from particle density and chemical elemental ratios:

$$\begin{aligned} \rho_{tot} &= f_1 \rho_1 + f_2 \rho_2 \\ f_1 + f_2 &= 1 \end{aligned} \quad [3]$$

$$\begin{aligned} R_{O/C} &= \chi_1 R_{O/C_1} + \chi_2 R_{O/C_2} \\ \chi_1 + \chi_2 &= 1 \end{aligned} \quad [4]$$

0 Where $R_{O/C}$ is oxygen to carbon ratio from AMS measurement of tar ball particles, and calculated particulate volume and molar fraction are given below:

Table S3. Particulate molar and volume fractions of bulk polar and nonpolar tar

Polar:Nonpolar prepared solution ratio	O/C molar ratio	O/C retrieved molar mixing ratio	Density (g cm ⁻³)	density retrieved volume mixing ratio
1:0	0.44	1:0	1.329±0.021	1:0
2:1	0.39	2.8:1	1.298±0.022	1.8:1
1:1	0.36	1.4:1	1.285±0.019	0.98:1
1:2	0.3	1:2.8	1.274±0.013	1:1.72
0:1	0.25	0:1	1.242±0.005	0:1

5 Molecular weight for polar and nonpolar fractions were simplified as $M_{\text{bulk-polar}}$ and $M_{\text{bulk-nonpolar}}$, and mixture tar ball particles follow the function below:

$$\frac{\bar{M}}{\rho} = \frac{x_1 M_{\text{bulk-polar}}}{\rho_1} + \frac{x_2 M_{\text{bulk-nonpolar}}}{\rho_2} \quad [5]$$

$$\bar{M} = x_1 M_{\text{bulk-polar}} + x_2 M_{\text{bulk-nonpolar}}$$

And it was calculated as $M_{\text{bulk-nonpolar}} \approx 1.3 M_{\text{bulk-polar}}$

For convenience and clarity, wavelength-dependent RI for tar ball were exponential or power-law fitted, the results were showed in Figure S8 and corresponded parameters were summarized in Table S4:

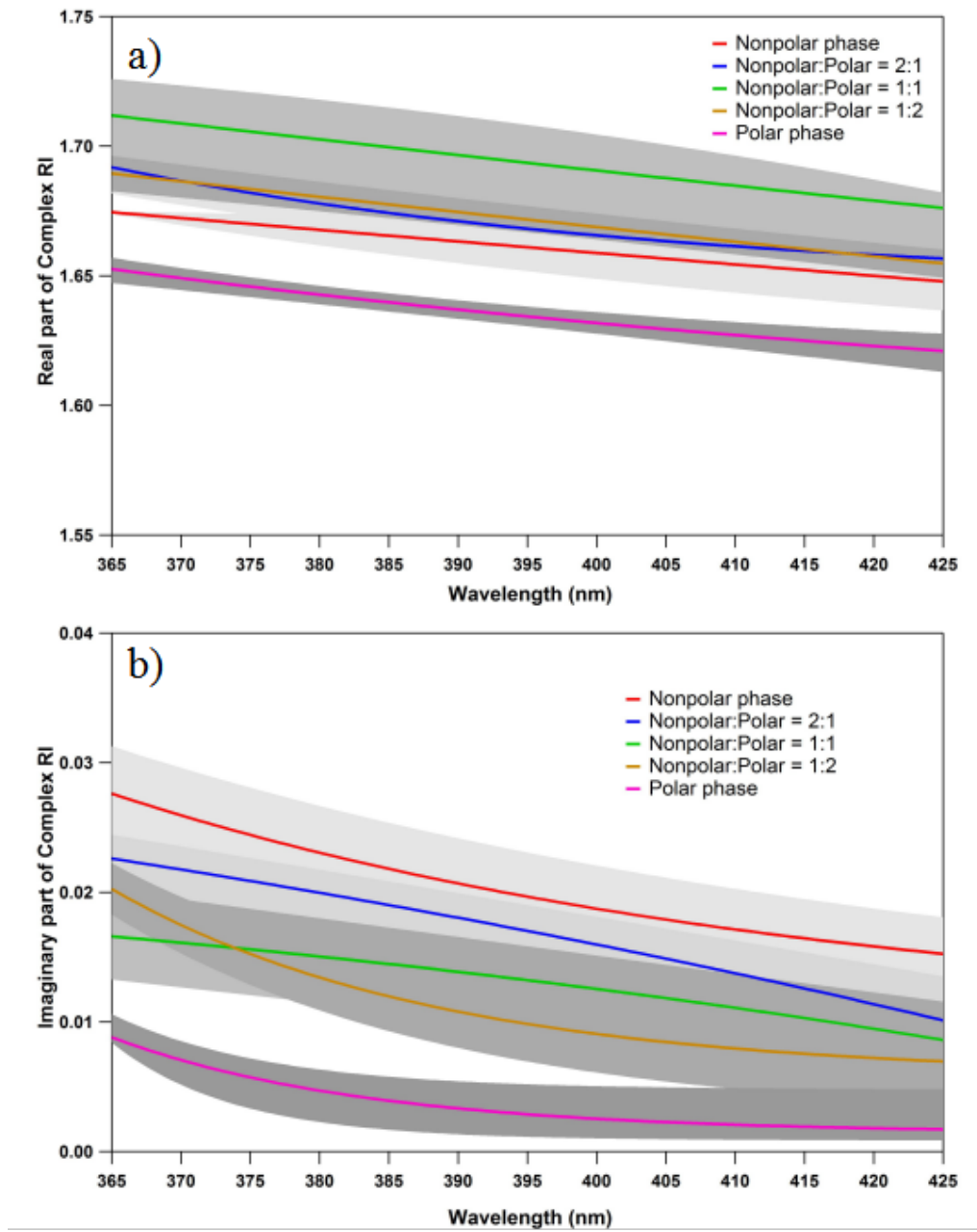


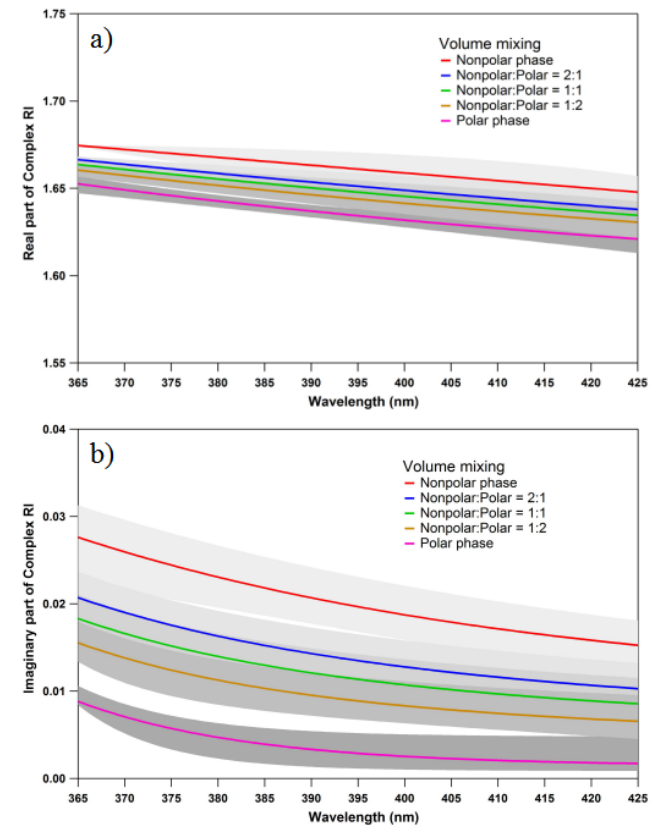
Figure S8. Regressed RI for tar ball particles of various mixing ratios: a) real part, and b) imaginary part

Table S4. Parameterization of the Wavelength-Dependent (365 to 425 nm) Effective Complex RI of tar ball particles

Tar ball		Real			Imaginary		
		Co	C1	C2	Co	C1	C2
Nonpolar phase	min	1.604	7.148	-1.27E-02	0.164	-8.89E-02	1.27E-03
	average	1.033	0.831	-7.08E-04	0.010	2.37E+01	-1.97E-02
	max	1.677	-1.95E-09	3.80E-02	0.010	8.75E+00	-1.65E-02
Nonpolar:polar 2:1	min	1.627	22.067	-1.65E-02	0.028	-1.05E-05	1.80E-02
	average	1.646	321.800	-2.43E-02	0.046	-1.81E-03	7.06E-03
	max	1.658	2819.637	-3.04E-02	0.330	-2.47E-01	5.86E-04
Nonpolar:polar 1:1	min	1.657	55.140	-1.98E-02	-0.291	3.52E-01	-4.01E-04
	average	1.324	0.697	-1.61E-03	0.023	-5.69E-16	5.10E+00
	max	1.754	-5.09E-18	6.145	-0.220	3.00E-01	-6.09E-04
Nonpolar:polar 1:2	min	1.832	-0.044	3.35E-03	0.002	6.88E+04	-4.19E-02
	average	1.306	0.683	-1.58E-03	0.006	8.43E+04	-4.27E-02
	max	1.550	0.826	-4.75E-03	0.009	1.56E+40	-1.64E+01
Polar phase	min	1.921	-0.133	1.97E-03	0.016	-5.83E-19	6.33E+00
	average	1.585	3.174	-1.06E-02	0.001	3.02E+06	-5.43E-02
	max	1.615	53.051	-1.95E-02	0.005	5.43E+11	-8.81E-02

5 Note: Non-shaded cells were fitted with an exponent; $n&k(\lambda)=C_0+C_1 \times e^{(C_2 \times \lambda)}$. Shaded cells were fitted with a power law; $n&k(\lambda)=C_0+ C_1 \lambda^{C_2}$

The calculated RI following “volume linear mixing rules” for tar ball were presented in Figure S9 and compared with experimental data in Figure S10.



0 **Figure S9.** Estimated RI for tar ball particles of various mixing ratios based on volume linear mixing rule: a) real part, and b) imaginary part

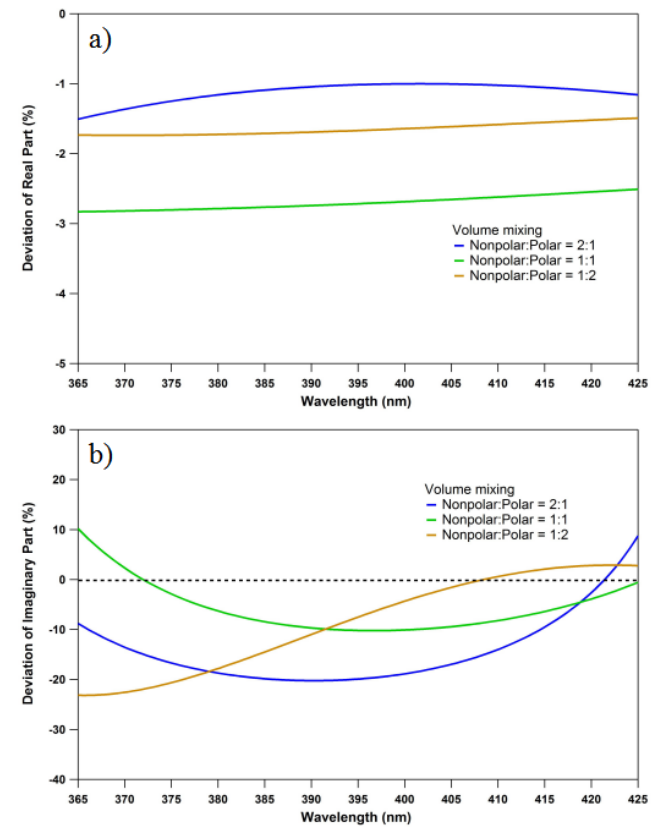


Figure S10. Deviation between experimental RI and predicted RI from volume linear mixing rule: a) real part, and b) imaginary part

The calculated RI following “molar fraction mixing rules” for tar ball were presented in Figure S11 and compared with experimental data in Figure S12.

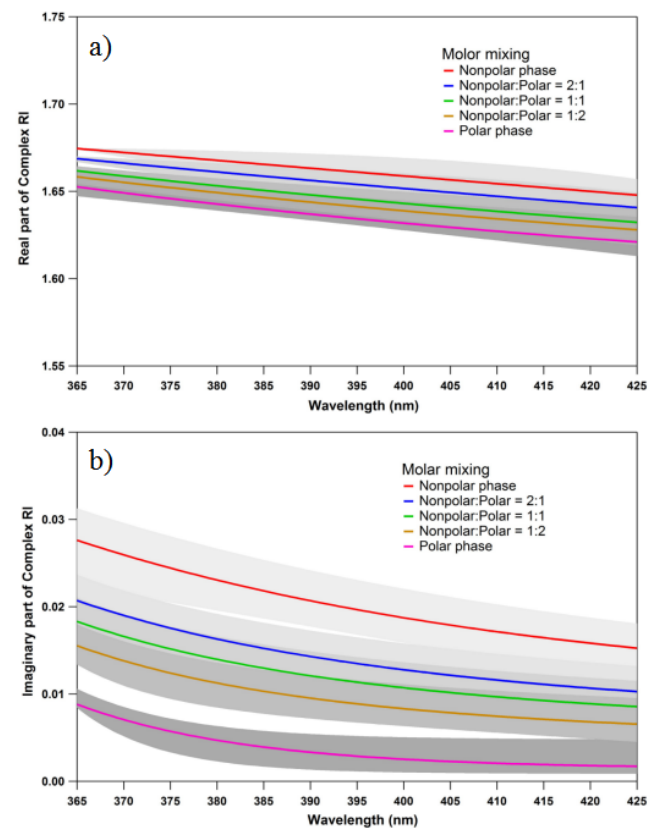


Figure S11. Estimated RI for tar ball particles of various mixing ratios based on molar fraction mixing rule: a) real part, and b) imaginary part

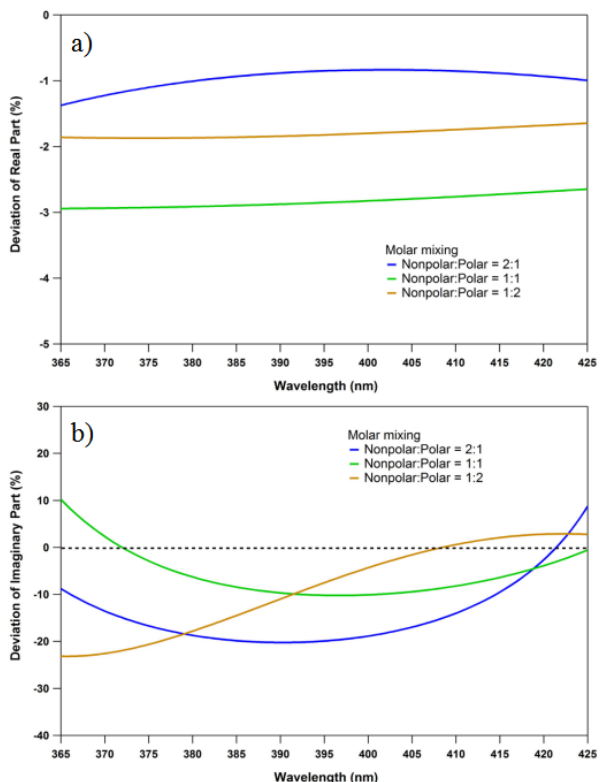


Figure S12. Deviation between experimental RI and predicted RI from molar fraction mixing rule: a) real part, and b) imaginary part

12. Summary of optical parameters for tar ball aerosol upon NO_x-dependent photochemical aging

Table S5. Summary of RI and Ångström exponent changes for tar ball particles upon photochemical oxidation (mean ± standard deviation)

Tar ball	Complex Refractive index			SSA (average)	Å _{abs}	Å _{abs_UVVIS}	Å _{ext}
	Average	375nm	405nm				
Fresh	(1.661±0.008)+(0.020±0.004)i	(1.671±0.003)+(0.025±0.003)i	(1.659±0.011)+(0.017±0.002)i	0.89 ± 0.01	5.87 ± 0.37	6.74	3.81 ± 0.18
O_0.7	(1.641±0.010)+(0.014±0.006)i	(1.652±0.001)+(0.021±0.001)i	(1.635±0.001)+(0.010±0.002)i	0.92 ± 0.02	9.33 ± 3.38	6.11	4.21 ± 0.07
O_1.7	(1.639±0.011)+(0.008±0.005)i	(1.651±0.002)+(0.015±0.004)i	(1.631±0.002)+(0.005±0.003)i	0.96 ± 0.03	10.96 ± 3.23	6.46	4.33 ± 0.04
O_3.9	(1.632±0.010)+(0.007±0.004)i	(1.643±0.001)+(0.011±0.002)i	(1.628±0.002)+(0.004±0.001)i	0.96 ± 0.02	10.63 ± 3.17	6.31	4.11 ± 0.09
O_6.7	(1.624±0.007)+(0.007±0.003)i	(1.630±0.003)+(0.009±0.003)i	(1.623±0.002)+(0.004±0.003)i	0.96 ± 0.02	9.89 ± 2.59	6.02	3.74 ± 0.06
N_0.5	(1.635±0.011)+(0.015±0.004)i	(1.646±0.001)+(0.018±0.001)i	(1.629±0.001)+(0.012±0.002)i	0.91 ± 0.01	6.92 ± 1.35	6.41	4.01 ± 0.07
N_2.0	(1.648±0.008)+(0.019±0.004)i	(1.653±0.002)+(0.025±0.003)i	(1.645±0.002)+(0.016±0.001)i	0.89 ± 0.01	5.60 ± 0.69	6.35	3.76 ± 0.10

13. Methanol extractable BrC mass absorption cross sections (MAC) for NO_x-free photochemical aged tar ball aerosols from 360 to 450 nm

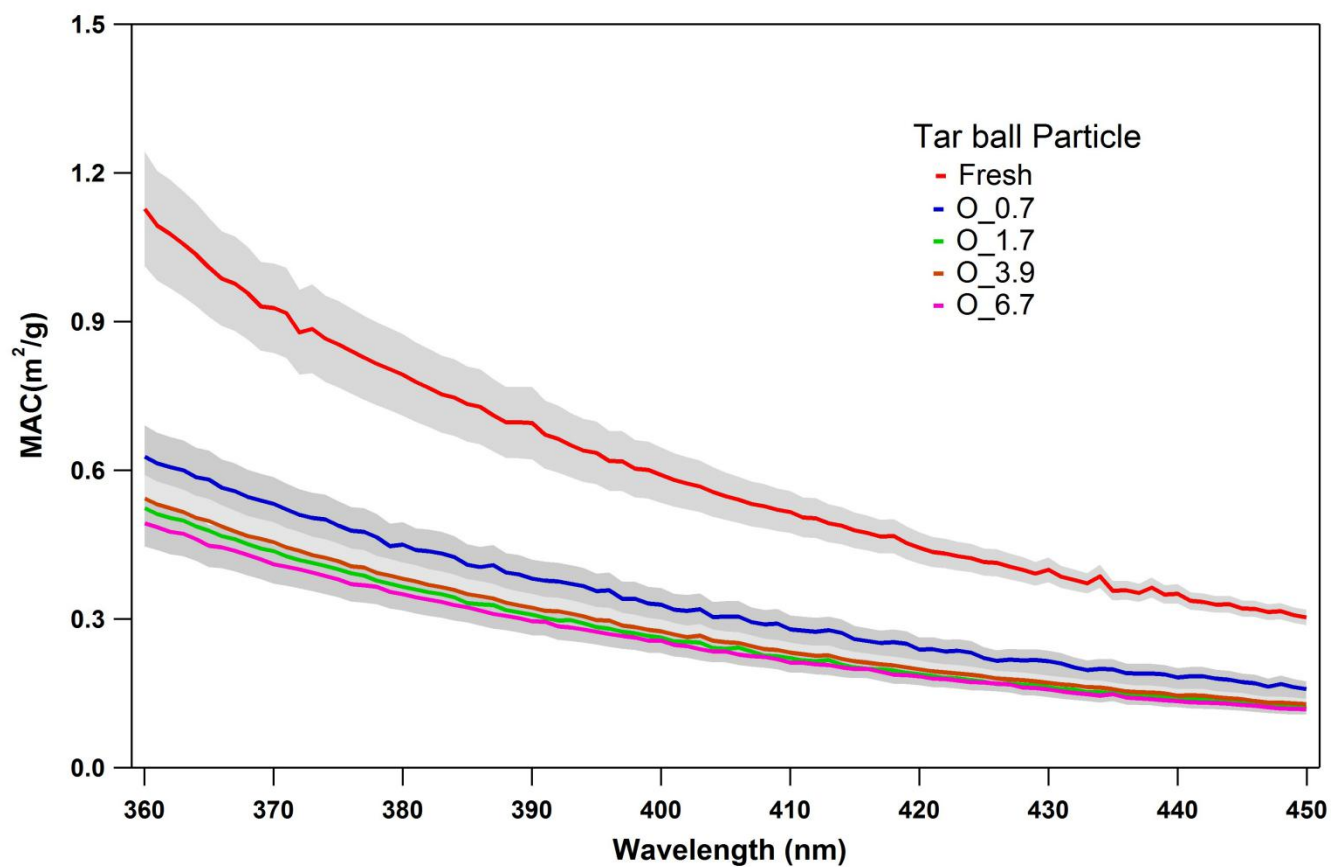


Figure S13. Diminishing in tar ball BrC mass absorption cross section (MAC) upon daytime NO_x-free photochemical oxidation

14. Optical and chemical changes for tar ball aerosols due to photolysis from UV light irradiation in the OFR

Studies have reported that BrC formation and SOA decomposition due to directly UV/near UV-short visible light irradiation of various precursors in both liquid and air (Bateman et al., 2011; Malecha and Nizkorodov, 2016; Wong et al., 2017). During photochemical aging through the OFR at residence time of 144s, tar ball particles were also exposed to high photon flux at 254 nm. We performed several experiments to estimate the influence of UV illumination on tar ball evolution. Irradiation tests of P1 and P2 repeated the same aging process of O_1.7 and O_3.9 without external O₃, and P3 was conducted at a full power of the UV lamps in the OFR. We observed slight chemical composition changes in the tar ball aerosols due to photolysis, as the O/C ratio continuously increased while H/C decreased with extension of irradiation (Table S6 and Figure S14). The O/C ratio increased by 0.04 for maximal irradiation exposure, which was much smaller than that from photochemical oxidation. This indicates that OH-initiated oxidation rather than photolysis reactions play a more dominant role in tar ball aging.

The decrease of the H/C ratio due to photolysis exhibited a distinct different chemical pathway than by OH photooxidation. According to the mass spectra analysis, particularly for the P3 experiment shown in Figure S14, the fractions of signals attributed to C_xH_y⁺ and C_xH_yO_z⁺ fragments decreased, and as a consequence, the contribution of the C_xH_yO⁺ fractions increased in photolyzed tar ball aerosols. Comparing to the fresh tar ball mass spectra, alkyl/alkenyl chains, carboxylic acids/peroxides (CO₂⁺, CHO₂⁺), and carbonyl/aldehyde groups (CO⁺, CHO⁺, C₂H₃O⁺) fragments depleted due to irradiation by UV light. Furthermore, increase of the *f*₄₄/*f*₄₃ ratio with photolysis shown in Figure S14, indicates decay of CO₂⁺ to a less extent compared to the loss of C₂H₃O⁺. Photolysis occurs in the condensed phase as particles containing photolabile compounds that efficiently absorb light at actinic wavelengths. Oxygenated species such as carbonyls, carboxylic acids, and peroxides are more vulnerable to photolysis, especially in the UV. With cleavage of the oxygenated functional groups, molecules become more volatile and may desorb to the gas phase (Henry and Donahue, 2012). Considerable amount of VOCs productions, including small molecular acids, ketones, aldehydes (e.g., acetic acid, formic acid, acetaldehyde, acetone, etc.), and hydrocarbon species (e.g., methane, ethene, propane, etc.), were detected from photo-degradation of various SOA (Malecha and Nizkorodov, 2016; Mang et al., 2008), and photocleavage of carbonyls has been emphasized in photolysis of SOA. Bateman et al. (2011) reported that exposure to UV irradiation increased the O/C ratio of dissolved ambient SOA, and they attributed the chemical changes to photodissociation of molecules containing carbonyl groups and net production of carboxylic acids that overweigh their decomposition in pH modified solution. Detailed mechanisms were proposed such as *n-π** Norrish type-I and -II splitting of carbonyls and *n-σ** photolysis of peroxides to form production of carboxylic acids in the presence of dissolved oxygen (Norrish, 1934; Pitts et al., 1964).

In the current experiments, photolysis occurred in particle phase which can be different from photolysis in liquid phase. First, the photolysis of particles should be less efficient as quenching is more likely and fragment caging can prevent rapid recombination. Second, photolysis products (volatile molecules and radicals) can more easily transfer to the gas phase rather than accumulate in the solution and be involved in further reactions. Epstein et al. (2014) isolated photolysis influence on α -pinene SOA. They reported suppression of SOA mass loading and marked decomposition of particle-bound organic peroxides from UV light illumination. The fraction of C_xH_y⁺ fragments slightly decreased while the oxygenated fragments increased upon irradiation. Wong et al. (2014) highlighted RH-dependent photolysis as a sink for SOA in the atmosphere, in particular, photolysis results in more oxidized SOA due to kinetic preference for degradation of less oxidized components, and they attributed the slower decay of *f*₄₄ (CO₂⁺) to photodissociation of peroxides and the formation of carboxylic acids in SOA upon UV irradiation.

The optical properties of SOA can change upon photolysis of photolabile carbonyl/carboxylic organics, peroxides, and other chromophores. Liu et al. (2016) investigated the influences of various environmental factors on light absorption of aromatic SOA from ozonolysis in the presence of NO_x. They suggested that photolysis, rather than hydrolysis, bleached SOA absorption due to degradation of nitrogen-containing chromophores. This conclusion was also confirmed by similar studies by Lee et al. (2014) and Aiona et al. (2018). In our study, the changes in the optical properties as a function of O/C ratio for tar balls upon photolysis are

shown in Figure S16. The relevant parameters are summarized in Table S7, MAC changes for tar ball upon photolysis are presented in Figure S17. RI of both real and imaginary parts weakly diminished during irradiation, and the average RI at 375 nm decreased by $0.012+0.006i$ for maximum photolyzed tar ball, corresponded MAC at 375 nm decreased by ~31.3%.

Table S6. Summary of mass spectra characters and effective density changes for tar ball particles upon photolysis from UV light irradiation (mean \pm standard deviation)

Tar ball	O:C	H:C	N:C	m/z>100 fraction	density
Fresh	0.25 \pm 0.01	1.55 \pm 0.01	0.012 \pm 0.002	0.32	1.24 \pm 0.01
P1	0.26 \pm 0.01	1.53 \pm 0.01	0.013 \pm 0.003	0.33	1.24 \pm 0.01
P2	0.27 \pm 0.01	1.51 \pm 0.01	0.011 \pm 0.001	0.32	1.24 \pm 0.01
P3	0.29 \pm 0.01	1.49 \pm 0.01	0.012 \pm 0.002	0.33	1.24 \pm 0.01

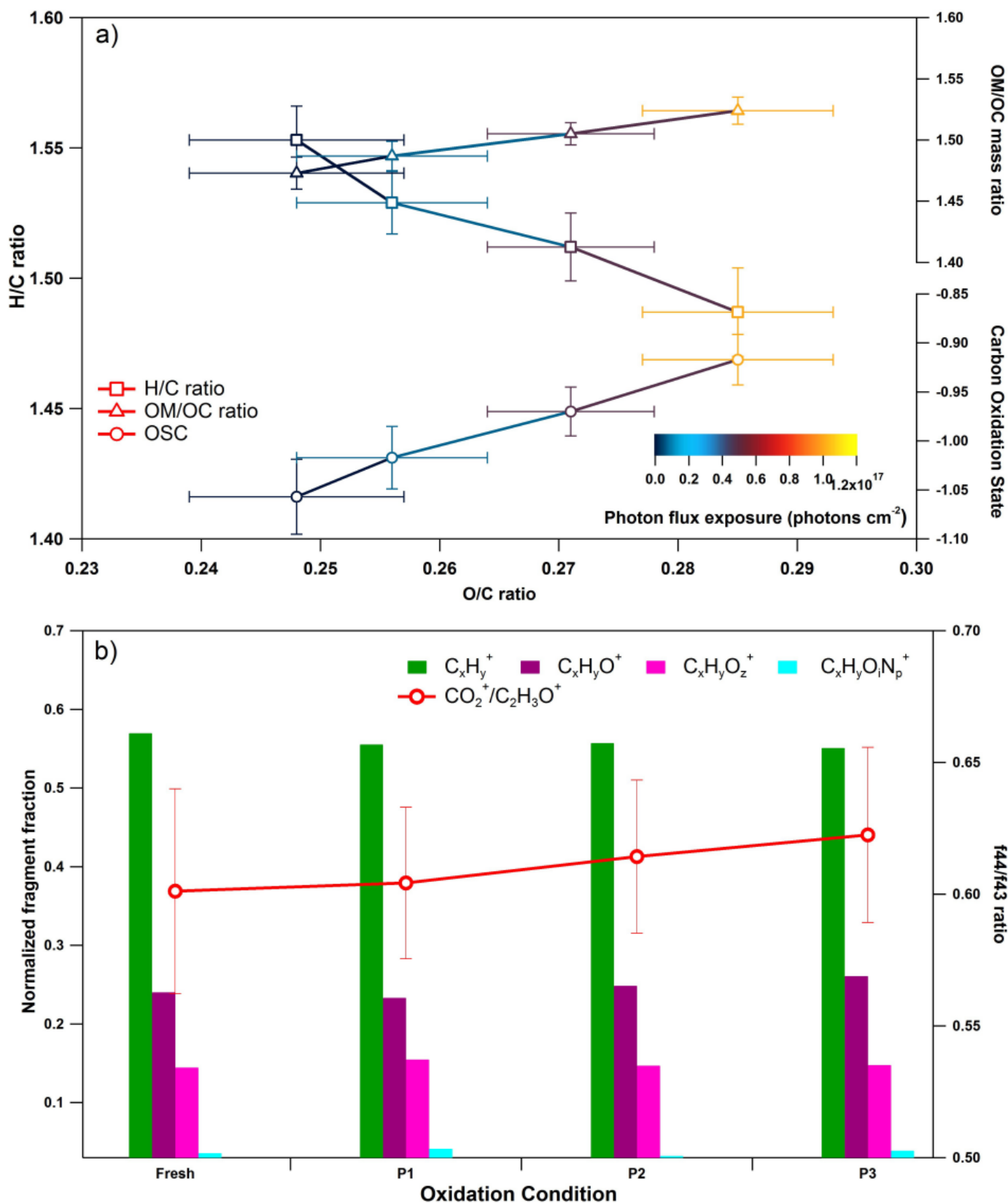


Figure S14. Dynamic changes for chemical characteristics of tar ball particle upon UV light irradiation: a) OM/OC, H/C ratio, and average carbon oxidation state (\overline{OSC}) changes as a function of O/C ratio; b) mass spectra evolution with photolysis extension in term of C_xH_y^+ , $\text{C}_x\text{H}_y\text{O}^+$, $\text{C}_x\text{H}_y\text{O}_z^+$, and $\text{C}_x\text{H}_y\text{O}_i\text{N}_p^+$ fragment groups

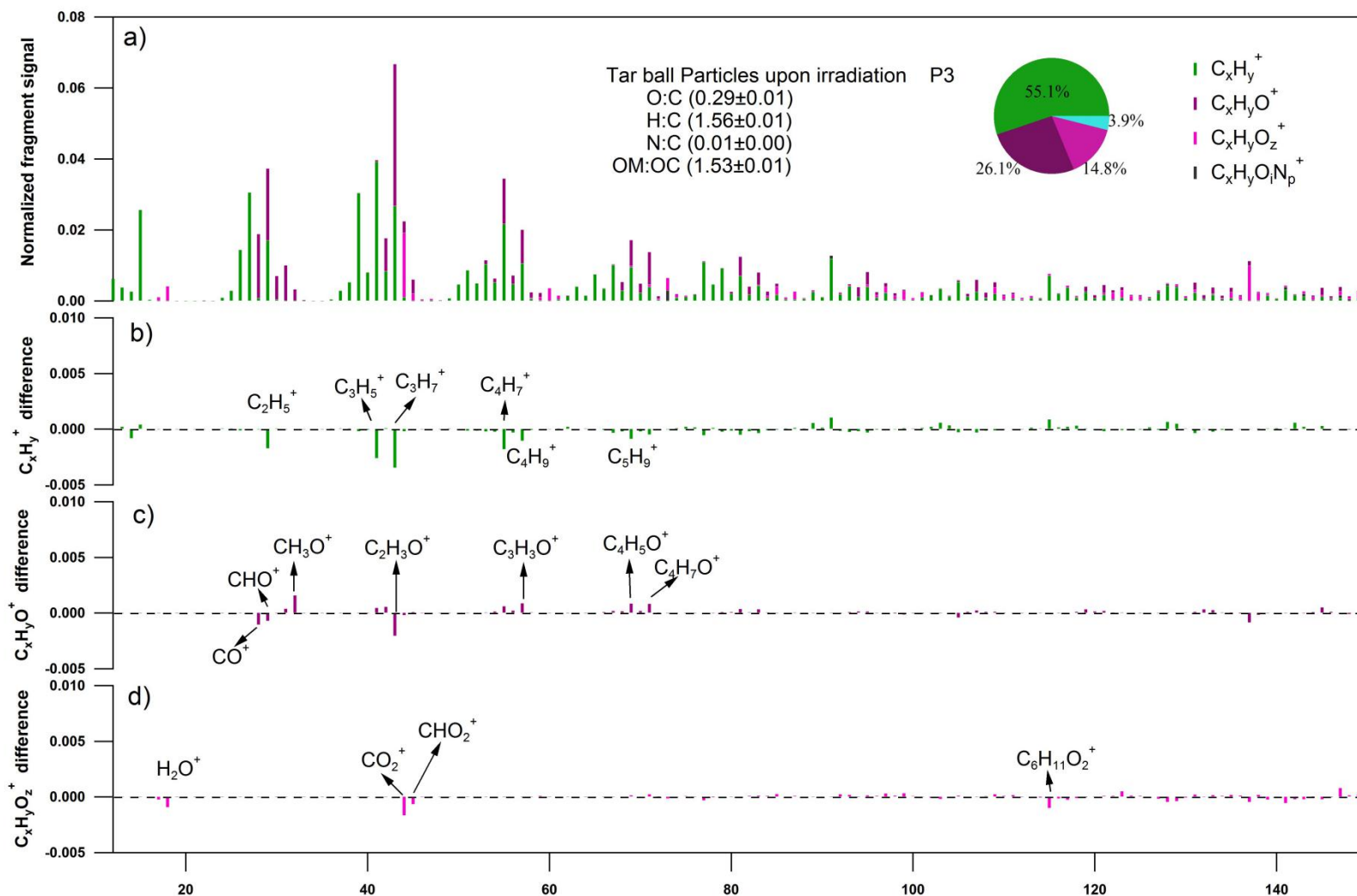


Figure S15. High-resolution mass spectra changes for nonpolar tar ball particles after maximum photolysis in P3 test, four ion groups were grouped for clarity as: $C_xH_y^+$, $C_xH_yO^+$, $C_xH_yO_z^+$ ($z > 1$), $C_xH_yO_iN_p^+$ ($i \geq 0, p \geq 1$). Ions O^+ , OH^+ , and H_2O^+ were included in the $C_xH_yO_z^+$ group. Mass fraction of the four fragment groups was pie-chart presented. a) normalized mass spectra of aged tar ball particles, b)–d) changes of $C_xH_y^+$, $C_xH_yO^+$, $C_xH_yO_z^+$, and $C_xH_yO_iN_p^+$ comparing with fresh tar ball normalized mass spectra

Table S7. Summary of RI and Ångström exponent changes for tar ball particles upon photolysis (mean ± standard deviation)

Tar ball	Complex Refractive index			SSA (average)	Å _{abs}	Å _{abs_UVVIS}	Å _{ext}
	Average	375nm	405nm				
Fresh	(1.661±0.008)+(0.020±0.004)i	(1.671±0.003)+(0.025±0.003)i	(1.659±0.011)+(0.017±0.002)i	0.89 ± 0.01	5.87 ± 0.37	6.74	3.81 ± 0.18
P1	(1.658±0.010)+(0.022±0.006)i	(1.668±0.001)+(0.027±0.001)i	(1.653±0.002)+(0.018±0.001)i	0.88 ± 0.02	6.92 ± 0.60	6.59	3.94 ± 0.03
P2	(1.649±0.008)+(0.018±0.004)i	(1.656±0.002)+(0.023±0.002)i	(1.647±0.002)+(0.014±0.003)i	0.90 ± 0.02	6.99 ± 1.22	6.50	3.79 ± 0.05
P3	(1.649±0.010)+(0.015±0.004)i	(1.659±0.005)+(0.019±0.004)i	(1.644±0.004)+(0.013±0.003)i	0.92 ± 0.01	7.42 ± 0.53	6.56	4.01 ± 0.01

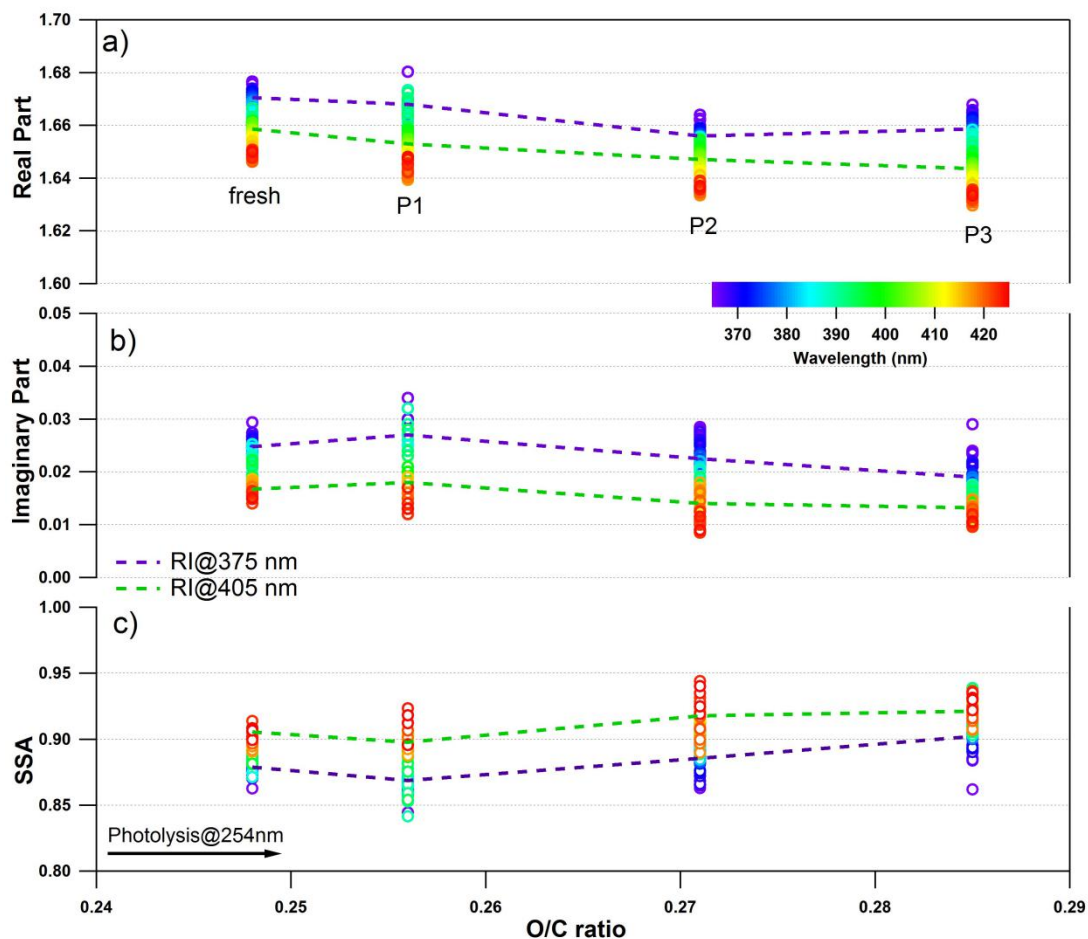


Figure S16. Changes in the retrieved spectral-dependent complex RI and SSA as a function of O/C ratio for tar ball particles upon 254 nm illumination: a) real part, b) imaginary part, and c) SSA calculated for 150 nm particles. The color scale shows the span in the RI for the wavelengths measured from 365 to 425 nm. For clarity, error bars for O/C ratio (± 0.01), RI (± 0.008 for real part, and ± 0.003 for imaginary part on average) and SSA (± 0.006) are not shown. The two dashed lines trace RI and SSA at 375nm (purple) and 405nm (green). P1~P3 represent photolysis studies with low to maximal photon flux exposures.

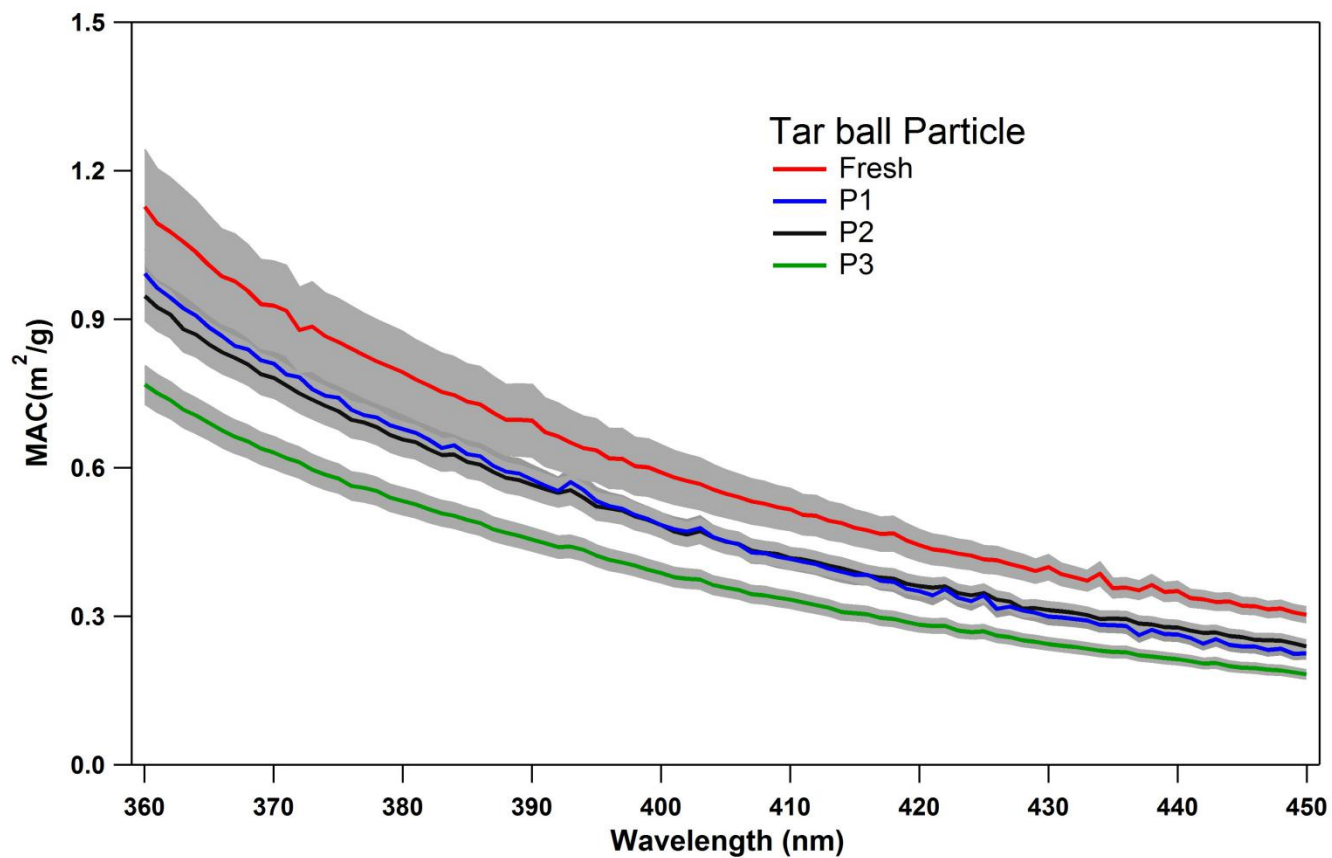


Figure S17. Changes of tar ball BrC mass absorption cross section (MAC) as a function of wavelength upon UV photolysis

15. Optical and chemical changes of tar ball aerosols due to O₃ oxidation

Prior to photochemical aging experiments, blank test of tar ball oxidation via O₃ under dark was conducted in the OFR. Initial environmental conditions (e.g., O₃ and tar balls concentrations, relative humidity, residence time, etc) were maintained the same with following daytime evolution simulations, while UV lamps were not turned on. Dynamic optical and chemical changes for tar balls were characterized and presented in Figure S18 and S19. We did not observe significant refractive index changes for tar balls after 28.6 ppm O₃ oxidation, taking ambient O₃ concentration of 50 ppb, equivalent atmospheric O₃ exposure for tar balls through the OFR was about one day. RIs of fresh tar ball are $(1.671 \pm 0.003) + (0.025 \pm 0.003)i$ and $(1.659 \pm 0.011) + (0.017 \pm 0.002)i$ at 375 and 405 nm, respectively. After O₃ oxidation, RIs became $(1.677 \pm 0.012) + (0.023 \pm 0.003)i$ and $(1.668 \pm 0.011) + (0.013 \pm 0.004)i$ at 375 and 405 nm, respectively. In Figure S19, O₃ oxidation weakly increased O/C and OM/OC ratios of tar balls, O/C ratio increased by 0.02 from initial 0.25, and OM/OC increased from 1.47 to 1.50, while H/C ratio remained during O₃ oxidation of tar ball particles. It was found C_xH_y⁺ fractions slight decreased in compensation of more C_xH_yO⁺ and C_xH_yO_z⁺ fragments formation, indicating oxygenated moieties produced.

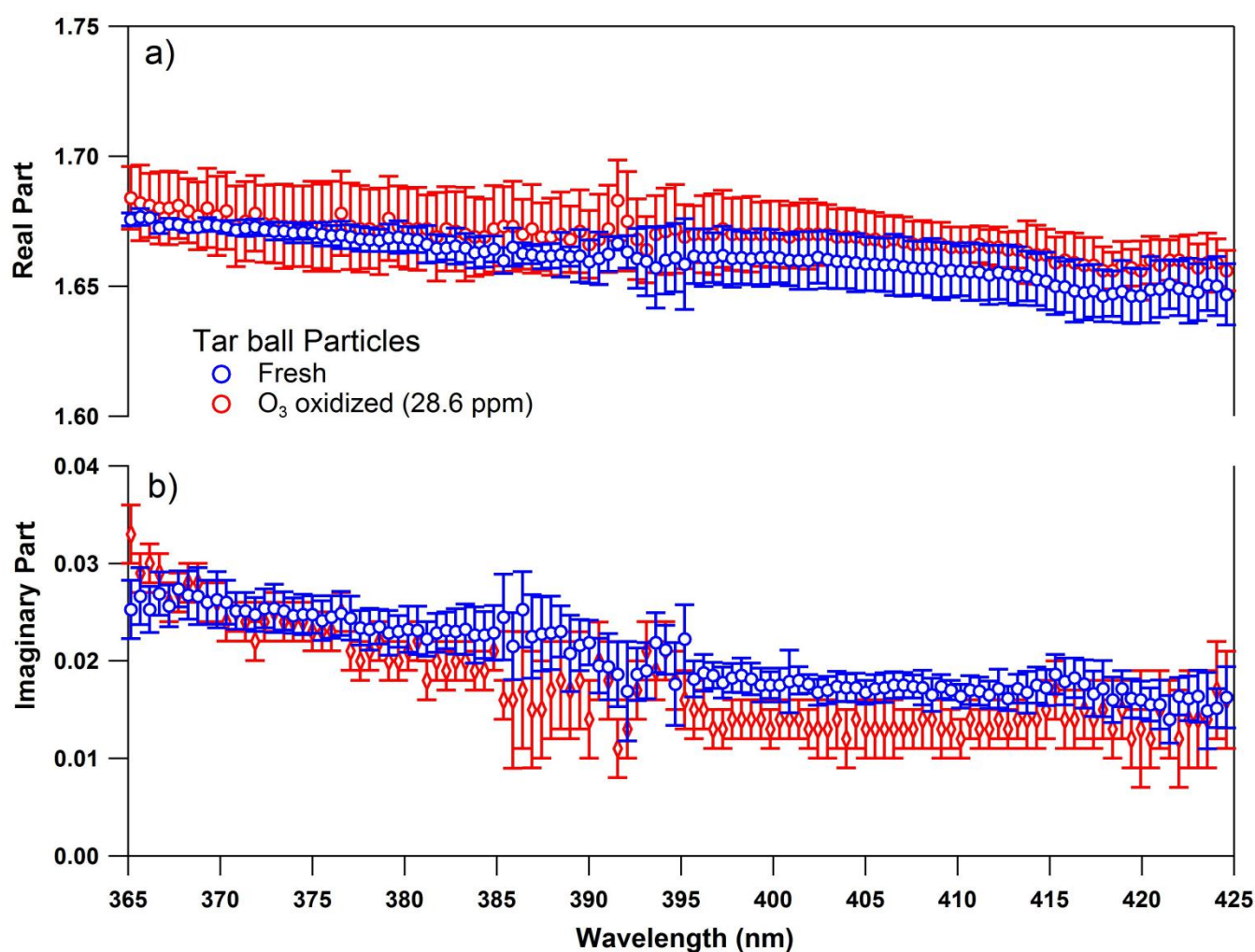


Figure S18. Refractive index as a function of wavelength for fresh and O₃ oxidized tar balls, a) real part, b) imaginary part

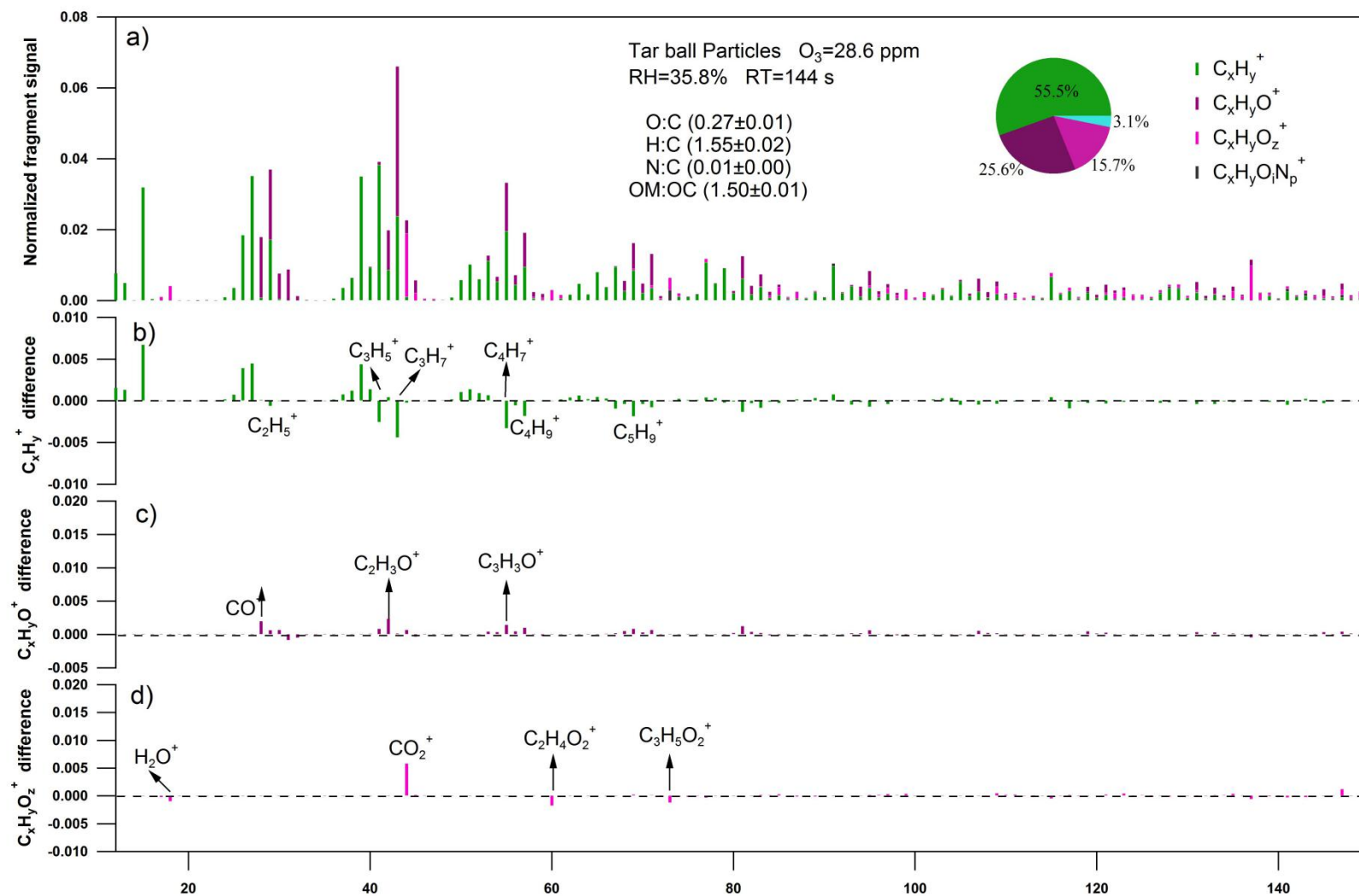


Figure S19. High-resolution mass spectral changes for nonpolar tar ball particles oxidized via O_3 . Four ion groups were grouped for clarity: $C_xH_y^+$, $C_xH_yO^+$, $C_xH_yO_z^+$ ($z>1$), $C_xH_yO_iN_p^+$ ($i\geq 0, p\geq 1$). Ions O^+ , OH^+ , and H_2O^+ were included in the $C_xH_yO_z^+$ group. Mass fraction of the four fragment groups was pie-chart presented. a) normalized mass spectra of O_3 oxidized tar ball particles, b)~d) changes of $C_xH_y^+$, $C_xH_yO^+$, $C_xH_yO_z^+$, and $C_xH_yO_iN_p^+$ comparing with fresh tar ball normalized mass spectra

16. Mass spectra characters and effective density changes for tar ball particles upon photochemical oxidation

Table S8. Summary of mass spectra characters and effective density changes for tar ball particles upon photochemical oxidation (mean \pm standard deviation)

Tar ball	O:C	H:C	N:C	m/z>100 fraction	density
Fresh	0.25 \pm 0.01	1.55 \pm 0.01	0.012 \pm 0.002	0.32	1.24 \pm 0.01
O_0.7	0.32 \pm 0.01	1.59 \pm 0.01	0.012 \pm 0.000	0.28	1.24 \pm 0.01
O_1.7	0.35 \pm 0.01	1.60 \pm 0.01	0.009 \pm 0.002	0.24	1.24 \pm 0.01
O_3.9	0.35 \pm 0.01	1.59 \pm 0.01	0.010 \pm 0.003	0.24	1.24 \pm 0.01
O_6.7	0.38 \pm 0.01	1.62 \pm 0.03	0.011 \pm 0.001	0.21	1.24 \pm 0.01
N_0.5	0.37 \pm 0.01	1.57 \pm 0.02	0.012 \pm 0.001	0.25	1.25 \pm 0.01
N_2.0	0.41 \pm 0.01	1.58 \pm 0.01	0.015 \pm 0.004	0.25	1.26 \pm 0.01

17. Detailed mass spectra changes for tar ball upon 6.7 EAD photochemical aging

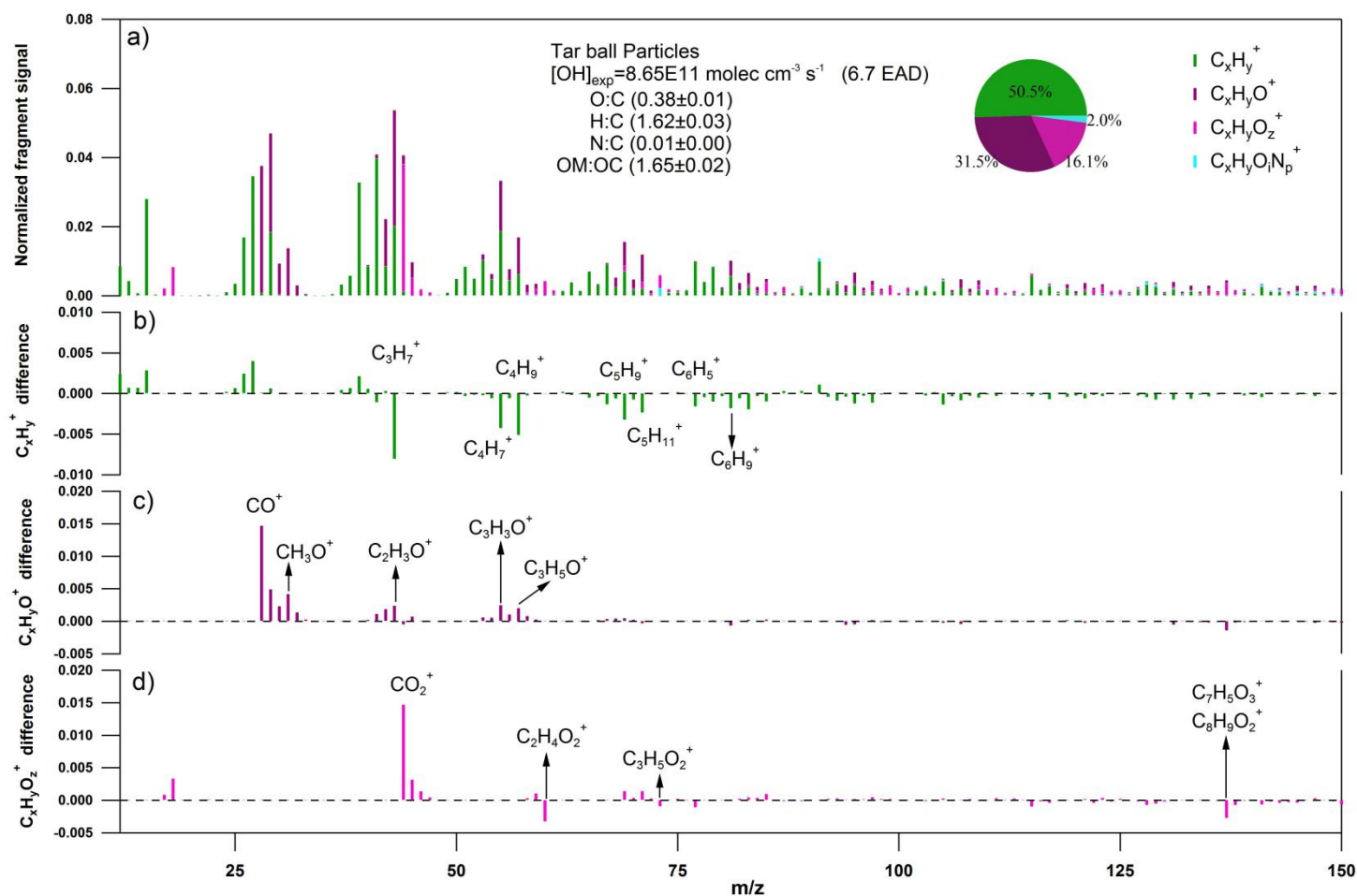


Figure S20. High-resolution mass spectral changes for nonpolar tar ball particles upon 6.7 EAD photochemical oxidation in absence of NO_x. Four ion groups were grouped for clarity: $C_xH_y^+$, $C_xH_yO^+$, $C_xH_yO_z^+$ ($z \geq 1$), $C_xH_yO_iN_p^+$ ($i \geq 0, p \geq 1$). Ions O^+ , OH^+ , and H_2O^+ were included in the $C_xH_yO_z^+$ group. Mass fraction of the four fragment groups was pie-chart presented. a) normalized mass spectra of 6.7 EAD aged tar ball particles, b)~d) changes of $C_xH_y^+$, $C_xH_yO^+$, $C_xH_yO_z^+$, and $C_xH_yO_iN_p^+$ comparing with fresh tar ball normalized mass spectra

18. Standard AMS spectra for inorganic salt of NH_4NO_3

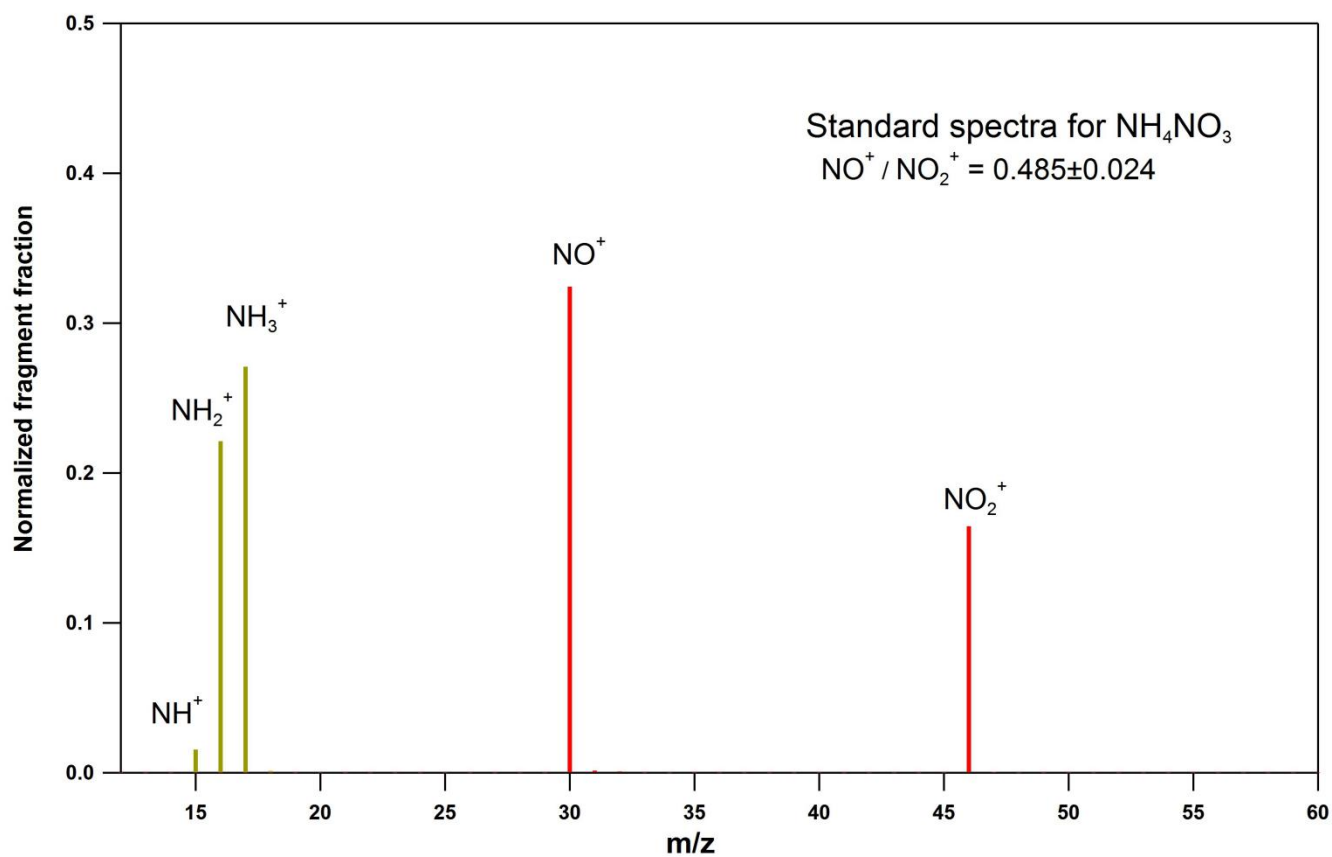


Figure S21. Standard mass spectra for NH_4NO_3 measured using HR-ToF-AMS system: NO^+ and NO_2^+ for nitrate, NH^+ , NH_2^+ , and NH_3^+ for ammonium

19. Detailed mass spectra changes for tar ball aerosols upon 4 EAD photochemical aging with 2.0 vol.% N₂O addition

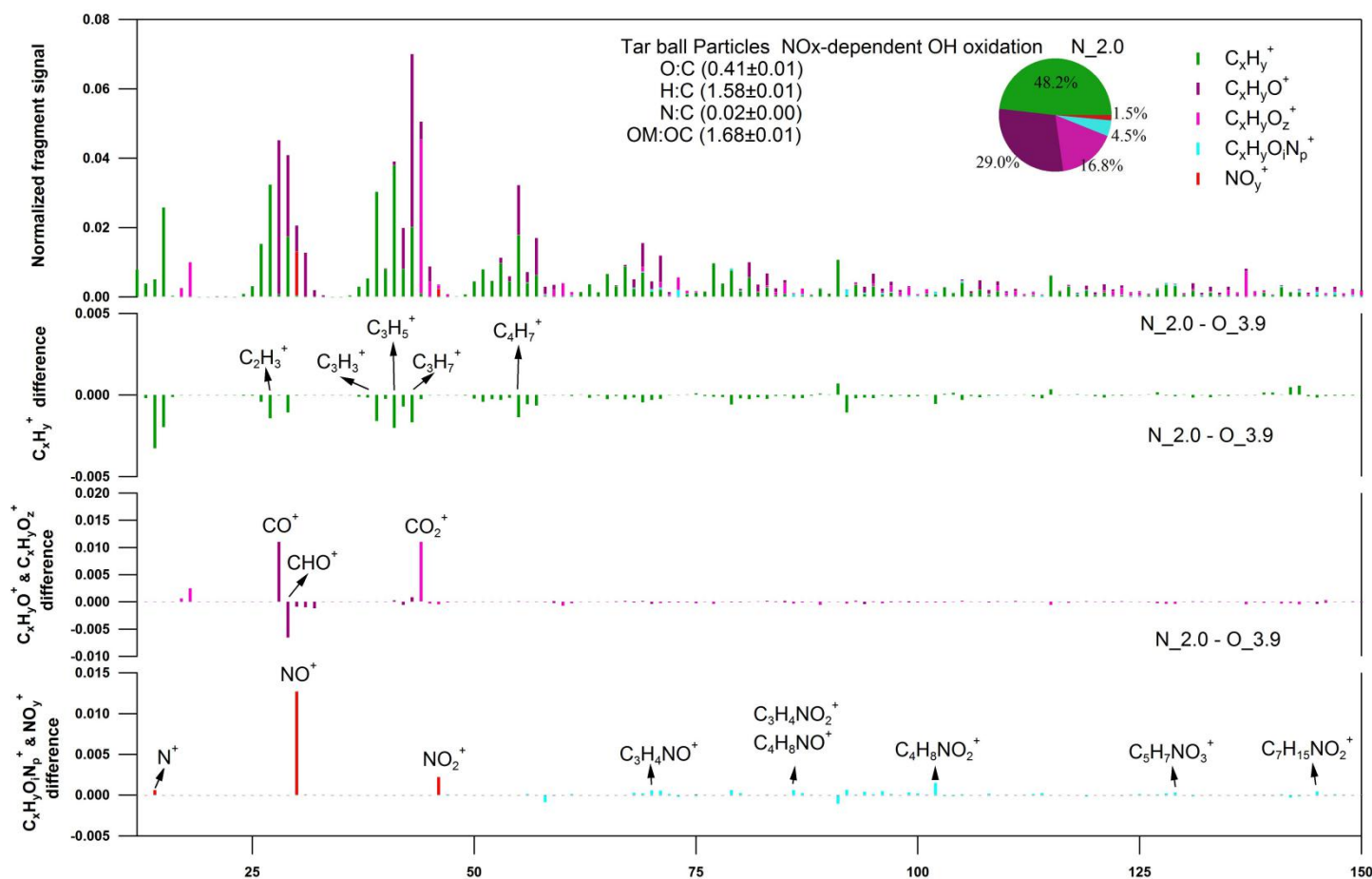
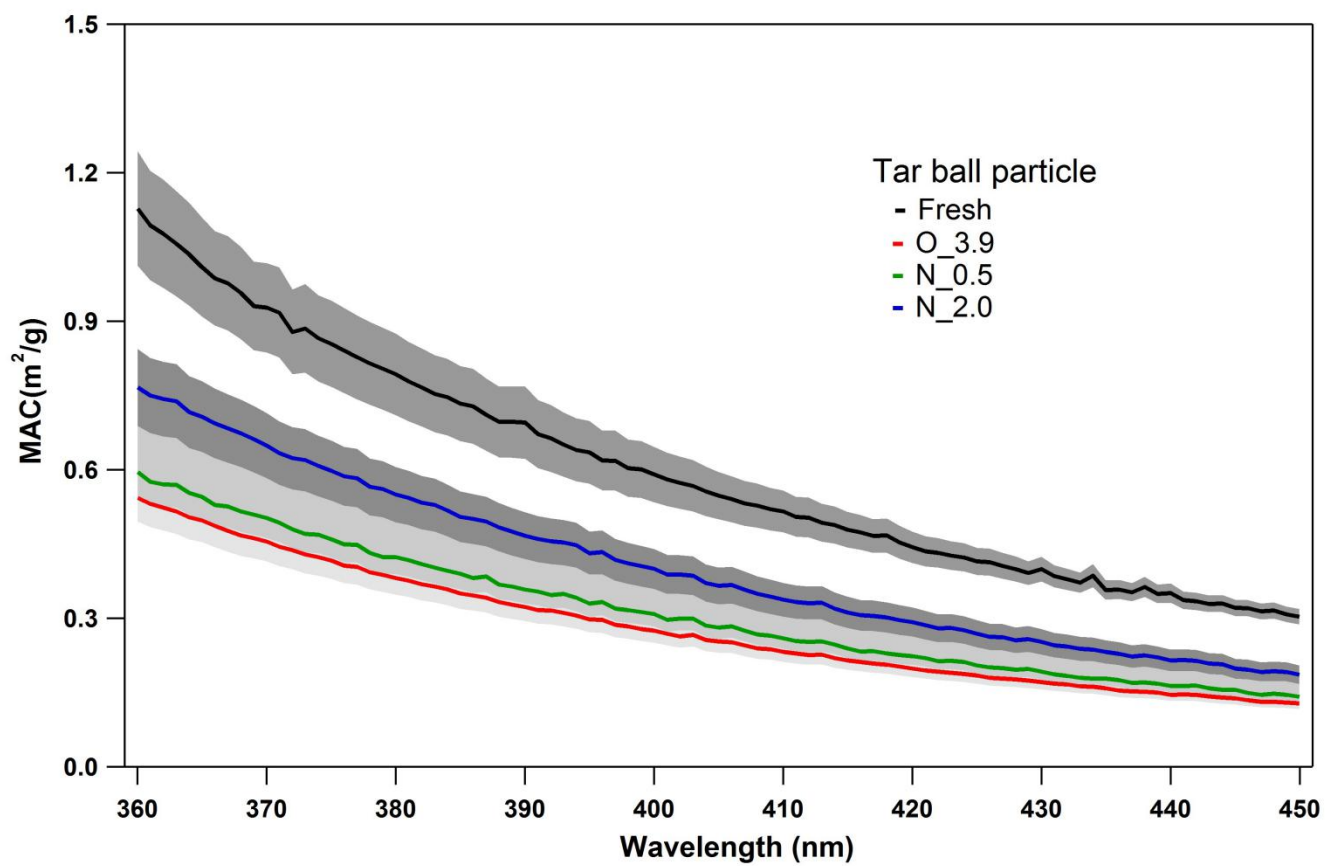


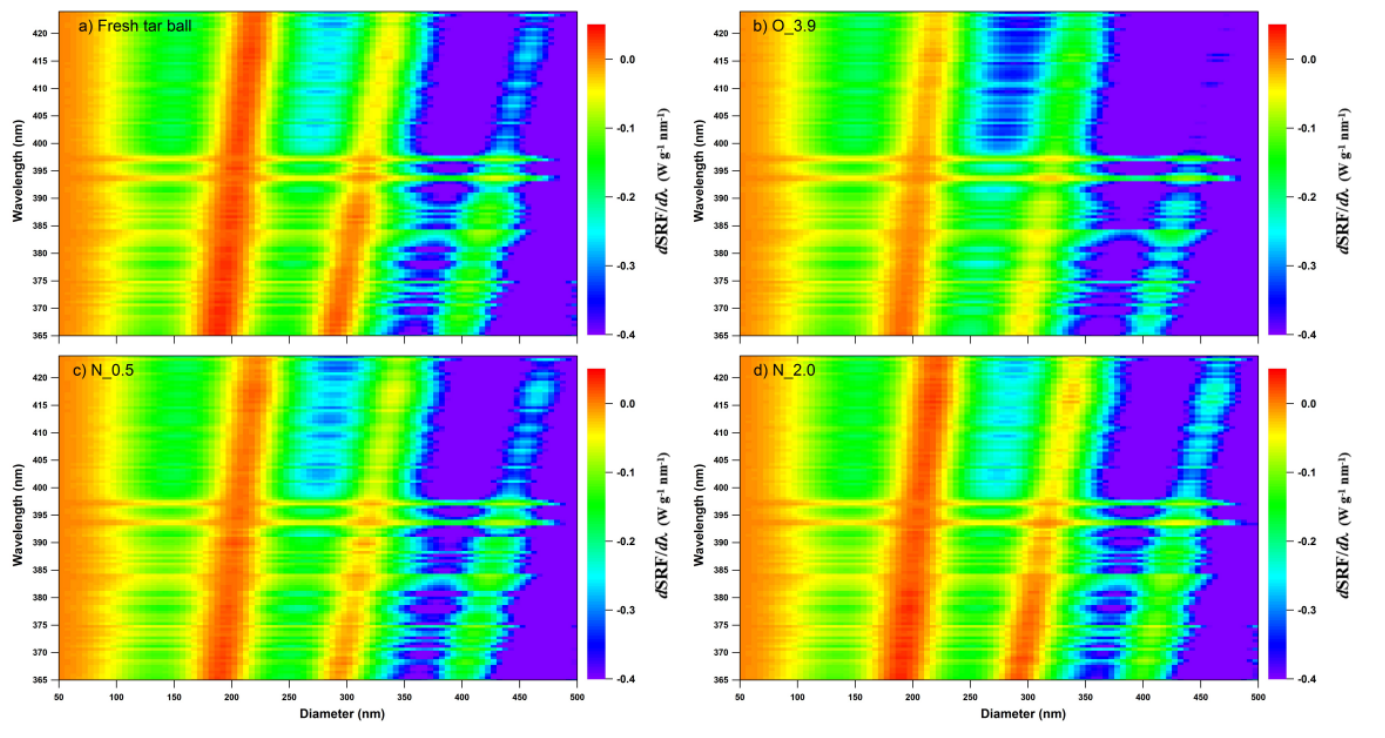
Figure S22. High-resolution mass spectra changes for nonpolar tar ball particles upon photochemical oxidation in presence of NO_x, five ion groups were grouped for clarity as: C_xH_y⁺, C_xH_yO⁺, C_xH_yO_z⁺ (z>1), C_xH_yO_iN_p⁺ (i≥0, p≥1), and NO_y⁺ (NO⁺ and NO₂⁺). Ions O⁺, OH⁺, and H₂O⁺ were included in the C_xH_yO_z⁺ group. Mass fraction of the four fragment groups was pie-chart presented. a) normalized mass spectra of aged tar ball particles, b)~d) changes of C_xH_y⁺, C_xH_yO⁺, C_xH_yO_z⁺, C_xH_yO_iN_p⁺, and NO_y⁺ comparing with photochemically oxidized tar ball in absence of NO_x.

1 20. Methanol extractable BrC mass absorption cross section (MAC) for tar ball aerosols upon various NO_x-dependent
2 photochemical aging processes

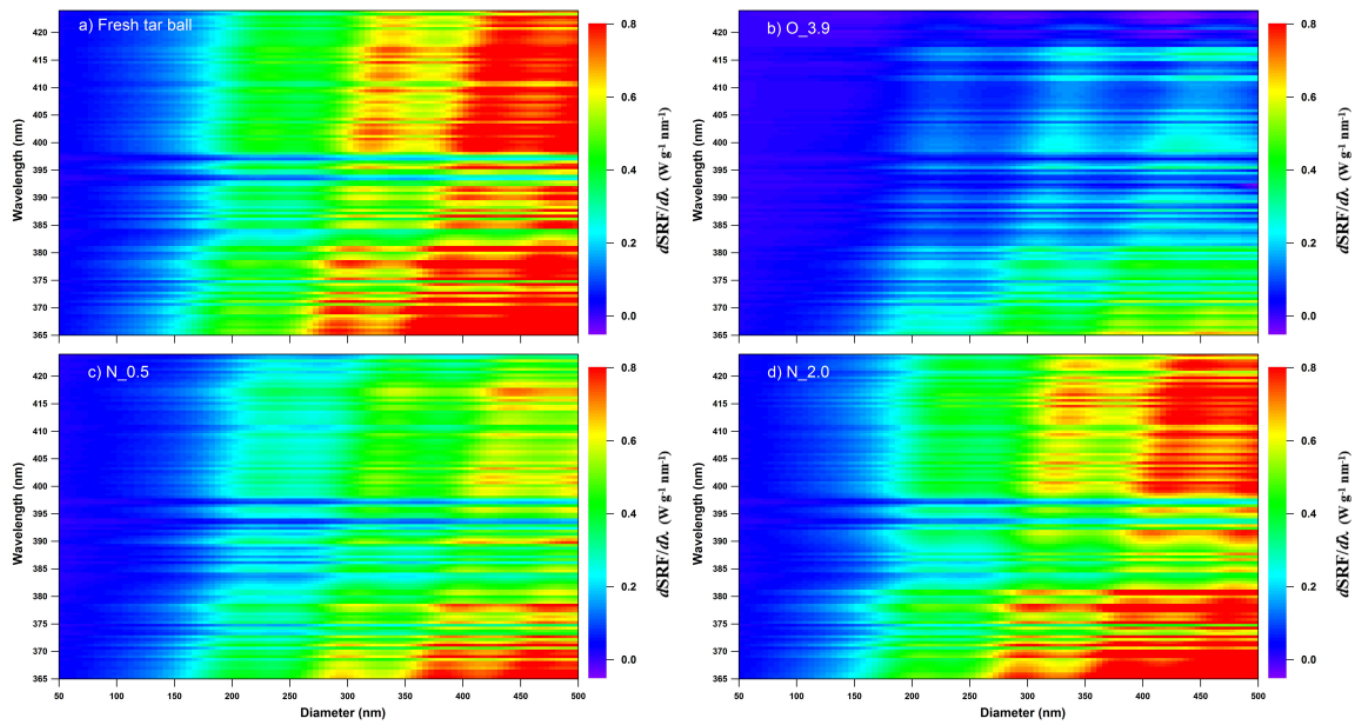


3
4 **Figure S23.** Methanol extractable BrC mass absorption cross section (MAC) for tar ball upon NO_x-dependent photochemical
5 oxidation as a function of wavelength
6

7 21. Particle size- and light wavelength-resolved radiative forcing for tar ball aerosols oxidized via various NO_x-dependent
8 oxidation processes



9
0 **Figure S24.** Ground based size-resolved radiative forcing spectra over solar irradiation of 365–425 nm for tar ball under various
1 oxidation: a) fresh tar ball, b) 3.9 EAD daytime photochemical oxidized tar ball, c) photooxidized tar ball with 0.5 vol.% N₂O
2 addition, d) photooxidized tar ball with 2.0 vol.% N₂O addition.
3



4

5

Figure S25. Snow based size-resolved radiative forcing spectra over solar irradiation of 365~425 nm for tar ball under various oxidation: a) fresh tar ball, b) 3.9 EAD OH initiated photochemical oxidized tar ball, c) photooxidized tar ball with 0.5 vol.% N₂O addition, d) photooxidized tar ball with 2.0 vol.% N₂O addition.

6

7

8

9

0 Reference

- 1 Adler, G., Flores, J. M., Abo Riziq, A., Borrmann, S., and Rudich, Y.: Chemical, physical, and optical evolution of biomass
2 burning aerosols: a case study, *Atmos. Chem. Phys.*, 11, 1491-1503, doi:10.5194/acp-11-1491-2011, 2011.
- 3 Aiken, A. C., Decarlo, P. F., Kroll, J. H., Worsnop, D. R., Huffman, J. A., Docherty, K. S., Ulbrich, I. M., Mohr, C., Kimmel,
4 J. R., and Sueper, D.: O:C and OM/OC ratios of primary, secondary, and ambient organic aerosols with high-resolution
5 time-of-flight aerosol mass spectrometry, *Environ. Sci. Technol.*, 42, 4478-4485, doi:10.1021/es703009q, 2008.
- 6 Aiona, P. K., Luek, J. L., Timko, S. A., Powers, L., Gonsior, M., and Nizkorodov, S. A.: Effect of Photolysis on Absorption
7 and Fluorescence Spectra of Light-Absorbing Secondary Organic Aerosols, *ACS Earth Space Chem.*, 2, 235-245,
8 doi:10.1021/acsearthspacechem.7b00153, 2018.
- 9 Andreae, M., and Gelencsér, A.: Black carbon or brown carbon? The nature of light-absorbing carbonaceous aerosols,
0 *Atmos. Chem. Phys.*, 6, 3131-3148, doi:10.5194/acp-6-3131-2006, 2006.
- 1 Arora, P., and Jain, S.: Estimation of organic and elemental carbon emitted from wood burning in traditional and improved
2 cookstoves using controlled cooking test, *Environ. Sci. Technol.*, 49, 3958-3965, doi:10.1021/es504012v, 2015.
- 3 Bateman, A. P., Nizkorodov, S. A., Laskin, J., and Laskin, A.: Photolytic processing of secondary organic aerosols dissolved
4 in cloud droplets, *Phys. Chem. Chem. Phys.*, 13, 12199-12212, doi:10.1039/C1CP20526A, 2011.
- 5 Bente, M., Sklorz, M., Streibel, T., and Zimmermann, R.: Online laser desorption-multiphoton postionization mass
6 spectrometry of individual aerosol particles: molecular source indicators for particles emitted from different traffic-related
7 and wood combustion sources, *Anal. Chem.*, 80, 8991-9004, doi:10.1021/ac801295f, 2008.
- 8 Bruns, E., Krapf, M., Orasche, J., Huang, Y., Zimmermann, R., Drinovec, L., Močnik, G., El-Haddad, I., Slowik, J., and
9 Dommen, J.: Characterization of primary and secondary wood combustion products generated under different burner loads,
0 *Atmos. Chem. Phys.*, 15, 2825-2841, doi:10.5194/acp-15-2825-2015, 2015.
- 1 Chakrabarty, R., Moosmüller, H., Chen, L. W., Lewis, K., Arnott, W., Mazzoleni, C., Dubey, M., Wold, C., Hao, W., and
2 Kreidenweis, S.: Brown carbon in tar balls from smoldering biomass combustion, *Atmos. Chem. Phys.*, 10, 6363-6370,
3 doi:10.5194/acp-10-6363-2010, 2010.
- 4 China, S., Mazzoleni, C., Gorkowski, K., Aiken, A. C., and Dubey, M. K.: Morphology and mixing state of individual
5 freshly emitted wildfire carbonaceous particles, *Nature communications*, 4, 2122, doi:10.1038/ncomms3122, 2013.
- 6 Chow, J. C., Watson, J. G., Robles, J., Wang, X., Chen, L.-W. A., Trimble, D. L., Kohl, S. D., Tropp, R. J., and Fung, K. K.:
7 Quality assurance and quality control for thermal/optical analysis of aerosol samples for organic and elemental carbon, *Anal.*
8 *Bioanal. Chem.*, 401, 3141-3152, doi:10.1007/s00216-011-5103-3, 2011.
- 9 Chýlek, P., Ramaswamy, V., and Cheng, R. J.: Effect of graphitic carbon on the albedo of clouds, *J. Atmos. Sci.*, 41,
0 3076-3084, doi:10.1175/1520-0469, 1984.

1 d'Almeida, G. A., Koepke, P., and Shettle, E. P.: Atmospheric aerosols: global climatology and radiative characteristics, A.
2 Deepak Publishing, Hampton, Va, 1991.

3 Epstein, S. A., Blair, S. L., and Nizkorodov, S. A.: Direct photolysis of α -pinene ozonolysis secondary organic aerosol:
4 effect on particle mass and peroxide content, *Environ. Sci. Technol.*, 48, 11251-11258, doi:10.1021/es502350u, 2014.

5 Hand, J. L., Malm, W., Laskin, A., Day, D., Lee, T.-b., Wang, C., Carrico, C., Carrillo, J., Cowin, J. P., and Collett, J.:
6 Optical, physical, and chemical properties of tar balls observed during the Yosemite Aerosol Characterization Study, *J.*
7 *Geophys. Res.: Atmos.*, 110, D21210, doi:10.1029/2004JD005728, 2005.

8 Han, Y., Han, Z., Cao, J., Chow, J., Watson, J., An, Z., Liu, S., and Zhang, R.: Distribution and origin of carbonaceous
9 aerosol over a rural high-mountain lake area, Northern China and its transport significance, *Atmos. Environ.*, 42, 2405-2414,
0 doi:10.1016/j.atmosenv.2007.12.020, 2008.

1 Han, Y., Lee, S., Cao, J., Ho, K., and An, Z.: Spatial distribution and seasonal variation of char-EC and soot-EC in the
2 atmosphere over China, *Atmos. Environ.*, 43, 6066-6073, doi:10.1016/j.atmosenv.2009.08.018, 2009.

3 He, L. Y., Lin, Y., Huang, X. F., Guo, S., Xue, L., Su, Q., Hu, M., Luan, S. J., and Zhang, Y. H.: Characterization of
4 high-resolution aerosol mass spectra of primary organic aerosol emissions from Chinese cooking and biomass burning,
5 *Atmos. Chem. Phys.*, 10, 11535-11543, doi:10.5194/acp-10-11535-2010, 2010.

6 Henry, K. M., and Donahue, N. M.: Photochemical aging of α -pinene secondary organic aerosol: effects of OH radical
7 sources and photolysis, *J. Phys. Chem. A*, 116, 5932-5940, doi:10.1021/jp210288s, 2012.

8 Hoffmann, D., Iinuma, Y., and Herrmann, H.: Development of a method for fast analysis of phenolic molecular markers in
9 biomass burning particles using high performance liquid chromatography/atmospheric pressure chemical ionisation mass
0 spectrometry, *J. Chromatography A*, 1143, 168-175, doi:10.1016/j.chroma.2007.01.035, 2007.

1 Jacobson, M. Z.: Analysis of aerosol interactions with numerical techniques for solving coagulation, nucleation,
2 condensation, dissolution, and reversible chemistry among multiple size distributions, *J. Geophys. Res.-Atmos.*, 107, D19,
3 4366, doi:10.1029/2001JD002044, 2002.

4 Jacobson, M. Z.: Effects of externally-through-internally-mixed soot inclusions within clouds and precipitation on global
5 climate, *J. Phys. Chem. A*, 110, 6860-6873, doi:10.1021/jp056391r, 2006.

6 Kim, K. H., Sekiguchi, K., Kudo, S., and Sakamoto, K.: Characteristics of Atmospheric Elemental Carbon (Char and Soot)
7 in Ultrafine and Fine Particles in a Roadside Environment, Japan, *Aerosol Air Qual. Res.*, 11, 1-12,
8 doi:10.4209/aaqr.2010.07.0061, 2011.

9 Lee, H. J., Aiona, P. K., Laskin, A., Laskin, J., and Nizkorodov, S. A.: Effect of solar radiation on the optical properties and
0 molecular composition of laboratory proxies of atmospheric brown carbon, *Environ. Sci. Technol.*, 48, 10217-10226,
1 doi:10.1021/es502515r, 2014.

- 2 Li, C., Hu, Y., Zhang, F., Chen, J., Ma, Z., Ye, X., Yang, X., Wang, L., Tang, X., and Zhang, R.: Multi-pollutant emissions
3 from the burning of major agricultural residues in China and the related health-economic effects, *Atmos. Chem. Phys.*, 17,
4 4957-4988, doi:10.5194/acp-17-4957-2017, 2017.
- 5 Li, Y., Huang, D., Cheung, H. Y., Lee, A., and Chan, C. K.: Aqueous-phase photochemical oxidation and direct photolysis of
6 vanillin-a model compound of methoxy phenols from biomass burning, *Atmos. Chem. Phys.*, 14, 2871-2885,
7 doi:10.5194/acp-14-2871-2014, 2014.
- 8 Li, Y. J., Yeung, J. W., Leung, T. P., Lau, A. P., and Chan, C. K.: Characterization of organic particles from incense burning
9 using an aerodyne high-resolution time-of-flight aerosol mass spectrometer, *Aerosol Sci. Tech.*, 46, 654-665,
0 doi:10.1080/02786826.2011.653017, 2012.
- 1 Li, S., Zhu, M., Yang, W., Tang, M., Huang, X., Yu, Y., Fang, H., Yu, X., Yu, Q., and Fu, X.: Filter-based measurement of
2 light absorption by brown carbon in PM_{2.5} in a megacity in South China, *Sci. Total Environ.*, 633, 1360-1369,
3 doi:10.1016/j.scitotenv.2018.03.235, 2018.
- 4 Liu, J., Lin, P., Laskin, A., Laskin, J., Kathmann, S. M., Wise, M., Caylor, R., Imholt, F., Selimovic, V., and Shilling, J. E.:
5 Optical properties and aging of light-absorbing secondary organic aerosol, *Atmos. Chem. Phys.*, 16, 12815-12827,
6 doi:10.5194/acp-16-12815-2016, 2016.
- 7 Malecha, K. T., and Nizkorodov, S. A.: Photodegradation of secondary organic aerosol particles as a source of small,
8 oxygenated volatile organic compounds, *Environ. Sci. Technol.*, 50, 9990-9997, doi:10.1021/acs.est.6b02313, 2016.
- 9 Mandalakis, M., Gustafsson, Ö., Alsberg, T., Egeback, A. L., Reddy, C. M., Xu, L., Klanova, J., Holoubek, I., and
0 Stephanou, E. G.: Contribution of biomass burning to atmospheric polycyclic aromatic hydrocarbons at three European
1 background sites, *Environ. Sci. Technol.*, 39, 2976-2982, doi:10.1021/es048184v, 2005.
- 2 Mang, S. A., Henricksen, D. K., Bateman, A. P., Andersen, M. P. S., Blake, D. R., and Nizkorodov, S. A.: Contribution of
3 carbonyl photochemistry to aging of atmospheric secondary organic aerosol, *J. Phys. Chem. A*, 112, 8337-8344,
4 doi:10.1021/jp804376c, 2008.
- 5 Ng, N., Canagaratna, M., Zhang, Q., Jimenez, J., Tian, J., Ulbrich, I., Kroll, J., Docherty, K., Chhabra, P., and Bahreini, R.:
6 Organic aerosol components observed in Northern Hemispheric datasets from Aerosol Mass Spectrometry, *Atmos. Chem.*
7 *Phys.*, 10, 4625-4641, doi:10.5194/acp-10-4625-2010, 2010.
- 8 Ng, N., Canagaratna, M., Jimenez, J., Chhabra, P., Seinfeld, J., and Worsnop, D.: Changes in organic aerosol composition
9 with aging inferred from aerosol mass spectra, *Atmos. Chem. Phys.*, 11, 6465-6474, doi:10.5194/acp-11-6465-2011, 2011.
- 0 Norrish, R. G.: Part II. Free radicals of short life: chemical aspects. A. General and inorganic. The primary photochemical
1 production of some free radicals, *Transactions of the Faraday Society*, 30, 103-113, 1934.

2 Passig, J., Schade, J., Oster, M., Fuchs, M., Ehlert, S., Jäger, C., Sklorz, M., and Zimmermann, R.: Aerosol mass
3 spectrometer for simultaneous detection of polyaromatic hydrocarbons and inorganic components from individual particles,
4 *Anal. Chem.*, 89, 6341-6345, doi:10.1021/acs.analchem.7b01207, 2017.

5 Pitts, J., Wan, J., and Schuck, E.: Photochemical studies in an alkali halide matrix. I. An o-nitrobenzaldehyde actinometer
6 and its application to a kinetic study of the photoreduction of benzophenone by benzhydrol in a pressed potassium bromide
7 disk, *J. Am. Chem. Soc.*, 86, 3606-3610, 1964.

8 Pósfai, M., Gelencsér, A., Simonics, R., Arató, K., Li, J., Hobbs, P. V., and Buseck, P. R.: Atmospheric tar balls: Particles
9 from biomass and biofuel burning, *J. Geophys. Res. Atmos.*, 109, D06213, doi:10.1029/2003JD004169, 2004.

0 Samburova, V., Connolly, J., Gyawali, M., Yatavelli, R. L., Watts, A. C., Chakrabarty, R. K., Zielinska, B., Moosmüller, H.,
1 and Khlystov, A.: Polycyclic aromatic hydrocarbons in biomass-burning emissions and their contribution to light absorption
2 and aerosol toxicity, *Sci. Total Environ.*, 568, 391-401, doi:10.1016/j.scitotenv.2016.06.026, 2016.

3 Santos, G. T., Santos, P. S., and Duarte, A. C.: Vanillic and syringic acids from biomass burning: Behaviour during
4 Fenton-like oxidation in atmospheric aqueous phase and in the absence of light, *J. Hazard. Mater.*, 313, 201-208,
5 doi:10.1016/j.jhazmat.2016.04.006, 2016.

6 Sedlacek III, A. J., Buseck, P. R., Adachi, K., Onasch, T. B., Springston, S. R., and Kleinman, L.: Formation and evolution
7 of Tar Balls from Northwestern US wildfires, *Atmos. Chem. Phys.*, 18, 11289-11301, doi:10.5194/acp-18-11289-2018,
8 2018.

9 Sumlin, B. J., Pandey, A., Walker, M. J., Pattison, R. S., Williams, B. J., and Chakrabarty, R. K.: Atmospheric
0 Photooxidation Diminishes Light Absorption by Primary Brown Carbon Aerosol from Biomass Burning, *Environ. Sci.*
1 *Technol. Lett.*, 4, 540-545, doi:10.1021/acs.estlett.7b00393, 2017.

2 Sumlin, B. J., Oxford, C. R., Seo, B., Pattison, R. R., Williams, B. J., and Chakrabarty, R. K.: Density and homogeneous
3 internal composition of primary brown carbon aerosol, *Environ. Sci. Technol.*, 52, 3982-3989, doi:10.1021/acs.est.8b00093,
4 2018.

5 Takahama, S., Johnson, A., Morales, J. G., Russell, L. M., Duran, R., Rodriguez, G., Zheng, J., Zhang, R., Toom-Sauntry, D.,
6 and Leaitch, W. R.: Submicron organic aerosol in Tijuana, Mexico, from local and Southern California sources during the
7 CalMex campaign, *Atmos. Environ.*, 70, 500-512, doi:10.1016/j.atmosenv.2012.07.057, 2013.

8 Tang, I. N.: Thermodynamic and optical properties of mixed-salt aerosols of atmospheric importance, *J. Geophys. Res.*
9 *Atmos.*, 102, 1883-1893, doi:10.1029/96JD03085, 1997.

0 Tivanski, A. V., Hopkins, R. J., Tyliczszak, T., and Gilles, M. K.: Oxygenated interface on biomass burn tar balls determined
1 by single particle scanning transmission X-ray microscopy, *J. Phys. Chem. A*, 111, 5448-5458, doi:10.1021/jp070155u,
2 2007.

- 3 Veres, P., Roberts, J. M., Burling, I. R., Warneke, C., de Gouw, J., and Yokelson, R. J.: Measurements of gas-phase
4 inorganic and organic acids from biomass fires by negative-ion proton-transfer chemical-ionization mass spectrometry, *J.*
5 *Geophys. Res. Atmos.*, 115, doi:10.1029/2010JD014033, 2010.
- 6 Wong, J. P., Nenes, A., and Weber, R. J.: Changes in light absorptivity of molecular weight separated brown carbon due to
7 photolytic aging, *Environ. Sci. Technol.*, 51, 8414-8421, doi:10.1021/acs.est.7b01739, 2017.
- 8 Wong, J. P., Zhou, S., and Abbatt, J. P.: Changes in secondary organic aerosol composition and mass due to photolysis:
9 relative humidity dependence, *J. Phys. Chem. A*, 119, 4309-4316, doi:10.1021/jp506898c, 2014.
- 0 Yee, L., Kautzman, K., Loza, C., Schilling, K., Coggon, M., Chhabra, P., Chan, M., Chan, A., Hersey, S., and Crounse, J.:
1 Secondary organic aerosol formation from biomass burning intermediates: phenol and methoxyphenols, *Atmos. Chem.*
2 *Phys.*, 13, 8019-8043, doi:10.5194/acp-13-8019-2013, 2013.
- 3 Zhou, S., Collier, S., Jaffe, D. A., Briggs, N. L., Hee, J., Sedlacek III, A. J., Kleinman, L., Onasch, T. B., and Zhang, Q.:
4 Regional influence of wildfires on aerosol chemistry in the western US and insights into atmospheric aging of biomass
5 burning organic aerosol, *Atmos. Chem. Phys.*, 17, 2477-2493, doi:10.5194/acp-17-2477-2017, 2017.

6
7